01 Jan 2022

# Polybenzodiazine Aerogels: All-Nitrogen Analogues of Polybenzoxazines Synthesis, Characterization, and High-Yield Conversion to Nanoporous Carbons

Vaibhav A. Edlabadkar

Saidulu Gorla

Rushi U. Soni

A. B.M.Shaheen ud Doulah

*et. al. For a complete list of authors, see https://scholarsmine.mst.edu/chem_facwork/3212*



## Recommended Citation

V. A. Edlabadkar et al., "Polybenzodiazine Aerogels: All-Nitrogen Analogues of Polybenzoxazines Synthesis, Characterization, and High-Yield Conversion to Nanoporous Carbons," *Chemistry of Materials*, American Chemical Society, Jan 2022.
The definitive version is available at https://doi.org/10.1021/acs.chemmater.2c02797

CHEMISTRY OF MATERIALS

pubs.acs.org/cm

Article

# Polybenzodiazine Aerogels: All-Nitrogen Analogues of Polybenzoxazines—Synthesis, Characterization, and High-Yield Conversion to Nanoporous Carbons

Vaibhav A. Edlabadkar, Saidulu Gorla, Rushi U. Soni, A. B. M. Shaheen ud Doulah, Joseph Gloriod, Samuel Hackett, Nicholas Leventis,* and Chariklia Sotiriou-Leventis*

Cite This: *Chem. Mater.* 2023, 35, 432−446

Read Online

ACCESS | Metrics & More | Article Recommendations | Supporting Information

**ABSTRACT:** Tetrahydroquinazoline (THQ) was designed as an all-nitrogen analogue of main-stream benzoxazine monomers. THQ solutions in DMF gelled at 100 °C via HCl-catalyzed ring-opening polymerization to polybenzodiazine (PBDAZ) wet gels, which were dried in an autoclave with supercritical fluid $CO_2$ to aerogels. These as-prepared PBDAZ-100 aerogels undergo ring-fusion aromatization at 240 °C under $O_2$. This oxidized form is referred to as PBDAZ-240. Chemical identification of PBDAZ-100 and PBDAZ-240 relied on consideration of all nine possible polymerization pathways, in combination with elemental analysis, infrared and solid-state $^{13}C$ NMR spectroscopy, and $^{15}N$ NMR spectroscopy of aerogels from the selectively $^{15}N$-enriched THQ monomer. Fully oxidized PBDAZ-240 aerogels were carbonized at 800 °C under Ar to carbon aerogels with 61% w/w yield and with retention of the nanomorphology of the parent PBDAZ-100 aerogels. Direct pyrolysis of PBDAZ-100 at 800 °C, i.e., without prior oxidation, resulted in only 40% w/w yield and complete loss of the fine nanostructure. The evolution of PBDAZ-240 aerogels along pyrolysis toward carbonization was monitored using progressively higher pyrolysis temperatures from 300 to 800 °C under Ar. Aerogels received at 600 and 800 °C (referred to as PBDAZ-600 and PBDAZ-800, respectively) had relatively high surface areas (432 and 346 $m^2\ g^{-1}$, respectively), a significant portion of which (79% in both materials) was assigned to micropores. The new polymer aerogels, together with polybenzoxazine aerogels, comprise a suitable basis set for comparing N-rich versus O-rich porous carbons as adsorbers.

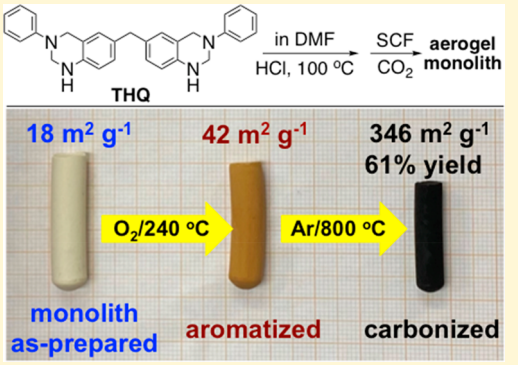


## 1. INTRODUCTION

Benzoxazines (BO) are cyclic mixed aminals/acetals of formaldehyde and were first reported in the mid-1940s.[1] Systematic polymerization studies were started much later by Ishida at Case Western Reserve University in the U.S. in the mid-1990s.[2] Today, polybenzoxanines (PBOs) are considered as a sub-class of phenolic resins, which is distinguished from other main-stream phenolic polymers such as, for example, those from the condensation of phenol, resorcinol, or phloroglucinol with formaldehyde, by the fact that they result from addition polymerization after the opening of the benzoxazine ring, and they use Mannich bridges ($-CH_2-N(Ph)-CH_2-$) rather than methylene ($-CH_2-$) or ether bridges ($-CH_2-O-CH_2-$) between their phenolic moieties. PBOs from Ishida's BO monomer (Scheme 1), the condensation product of bisphenol A, aniline, and formaldehyde, are considered the standard against which all other polybenzoxazines are compared with.[3] One of the desirable attributes of PBOs is that they are carbonizable in good yields.

On the other hand, aerogels are low-density nanostructured nanoporous solids.[4] They are prepared by drying sol−gel derived wet gels in a way that preserves nearly all of their volume into their final dry form. The most common drying method involves solvent exchange in an autoclave with liquid $CO_2$ that is subsequently converted into a supercritical fluid (SCF) and is vented off like a gas.[5] By definition, aerogels include porous carbons and ceramic materials that come from sol−gel-derived wet gels.[6] Due to their low densities and open porosity, aerogels exhibit low thermal conductivities and high acoustic impedance and are commercially available on an industrial scale for thermal and acoustic insulation.[7−9]

PBO aerogels were reported first by Lorjai in 2009 and were prepared via thermal gelation of Ishida's monomer (at 130 °C in xylene), followed by typical drying with SCF $CO_2$ and curing of the resulting aerogels in air at up to 200 °C, presumably to complete polymerization.[10,11] Curiously, the

Received: September 11, 2022
Revised: November 30, 2022
Published: January 3, 2023

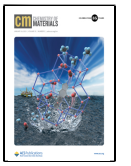

**Scheme 1. Molecular Comparison of Benzoxazine (BO) with its All-Nitrogen Analogue Tetrahydroquinazoline Monomer (THQ)**

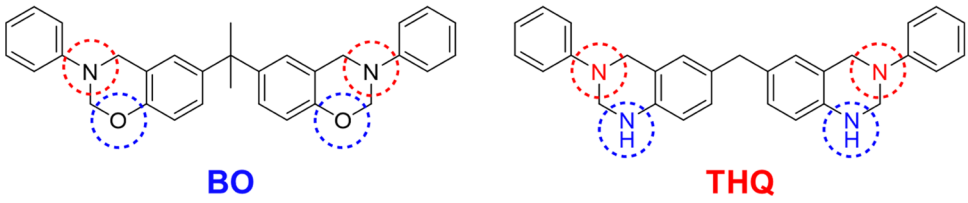


**Scheme 2. Synthesis of the Tetrahydroquinazoline (THQ) Monomer**

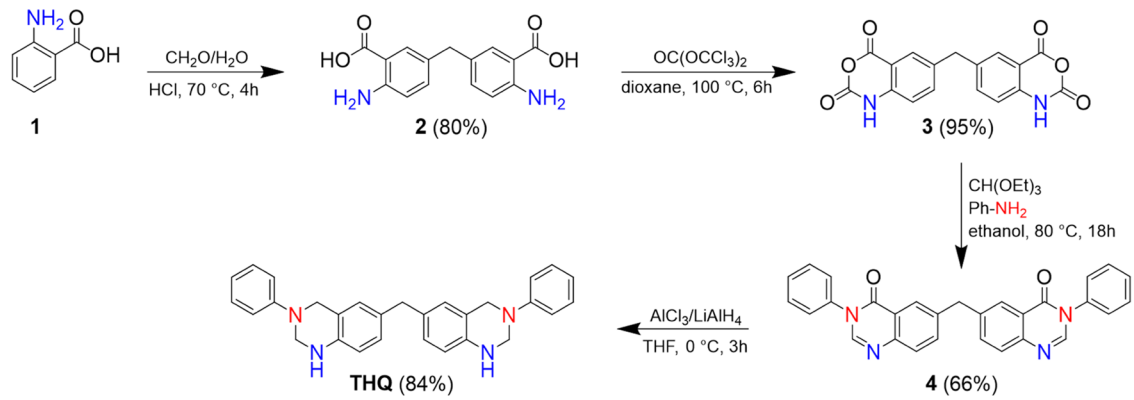


same authors also noted that the carbonization yield of PBOs in the aerogel form was higher than that of PBOs in the bulk form. With this background, in 2014, we introduced a new HCl-catalyzed room-temperature gelation method of Ishida's monomer, and it became possible to deconvolute polymerization from curing. Thus, it was discovered that in analogy to what takes place during the curing of polyacrylonitrile,[12,13] facile air circulation through the open porosity of the aerogel structure during curing causes oxidative ring-fusion aromatization of dangling anilines with main-chain phenols leading to the formation of fused heteroaromatic pyridinium rings along the polymeric backbone.[14−17] Pyrolysis of aromatized PBO aerogels at 800 °C under Ar yielded carbon aerogels with 61% yield versus only 27% without prior aromatization. These PBO-derived carbon aerogels contained 7.35% w/w of O and 5.24% w/w of N.

Reasoning by analogy to other carbon aerogels,[18−20] one possible application of PBO-derived carbon aerogels is in $CO_2$ sequestration. Yet, the $CO_2$ adsorption capacity, even of activated, surface-area-enhanced, microporous PBO carbon aerogels, remains relatively low ($3.26 \pm 0.13$ mmol $g^{-1}$).[21] It has been discussed that along with the porosity and surface structure, heteroatoms such as O and N may play a decisive role in the properties of porous carbon materials.[22] In particular, nitrogen-containing functional groups, e.g., in pyridinic and pyridonic positions, are responsible for adding basic character to the derived carbons,[23] which is thought to improve interaction with $CO_2$ for adsorption applications.[20,24−27] Along these lines, two main approaches have been used for introducing nitrogen in porous carbons: by post-treatment with nitrogen-containing molecules such as ammonia, urea, melamine, nitric acid, etc.[27] or by the *in situ* method, which relies on using nitrogen-containing polymeric carbon precursors, and involves a judicious choice of the polymerization chemistry and selection of monomers.[28]

Along the rationale of *in situ* doping, the tetrahydroquinazoline monomer (THQ) (Scheme 1, right) is a symmetric bis-cyclic aminal of formaldehyde and was specifically designed as an all-nitrogen alternative to Ishida's BO monomer. HCl-catalyzed ring-opening polymerization and gelation of THQ yield a new class of materials, which, in analogy to polybenzoxazines, are referred to as polybenzodiazine (PBDAZ) aerogels. However, unlike the ring-opening polymerization of benzoxazines, which starts with the protonation of "O", the ring opening of THQ has more options, resulting in a more complicated composition for PBDAZ. In terms of carbonization, PBDAZ aerogels behave similarly to their PBO analogues: high-yield carbonization requires prior oxidative ring-fusion aromatization along the main linear polymer chains. In this regard, the open-pore aerogel structure of PBDAZ offers the already familiar advantage of facile air circulation. Thus, the carbonization yield of PBDAZ at 800 °C reached 61% w/w, matching that of PBO. The elemental makeup of such PBDAZ-derived carbon aerogels included 7.13% w/w of N and 7.57% w/w of O. Thus, while the amount of oxygen was about the same as in aromatized and subsequently carbonized PBO (7.35%, see above), the amount of nitrogen in carbonized polybenzodiazine aerogels was significantly higher than that in PBO-derived carbon aerogels (5.24%).

## 2. RESULTS AND DISCUSSION

**2.1. Material Synthesis.** *2.1.1. Synthesis of THQ.* The THQ monomer was synthesized from commercially available anthranilic acid (**1**) in four steps, as illustrated in Scheme 2, using modified literature procedures. In the first step, two moles of anthranilic acid (**1**) were bridged with formaldehyde to 4,4′-methylene bis-anthranilic acid (**2**) via a HCl-catalyzed reaction.[29] In the second step, **2** was reacted with triphosgene to yield a bis(amide-anhydride) product **3**.[30] In the third step, **3** reacted with aniline and triethyl orthoformate in ethanol to


https://doi.org/10.1021/acs.chemmater.2c02797
Chem. Mater. 2023, 35, 432−446

give the bis(amide-imide) product **4**.[31] The final step involved the $AlCl_3$-catalyzed reduction of **4** with $LiAlH_4$ to yield bis(3-phenyl-1,2,3,4-tetrahydroquinazolin-6-yl) methane (THQ).[32] The crude product was purified by refluxing in methanol (see Section 4). For chemical characterization and mechanistic studies, three additional versions of THQ were prepared, one with $^{15}N$-enriched aniline, one with $^{15}N$-enriched anthranilic acid, and one with both reagents being $^{15}N$-enriched.

*2.1.2. Preparation of PBDAZ Aerogels.* As summarized in Scheme 3, gelation of 20% w/w THQ solutions in DMF was

**Scheme 3. Processing of THQ through Gelation, Drying, Air Oxidation, and Carbonization**

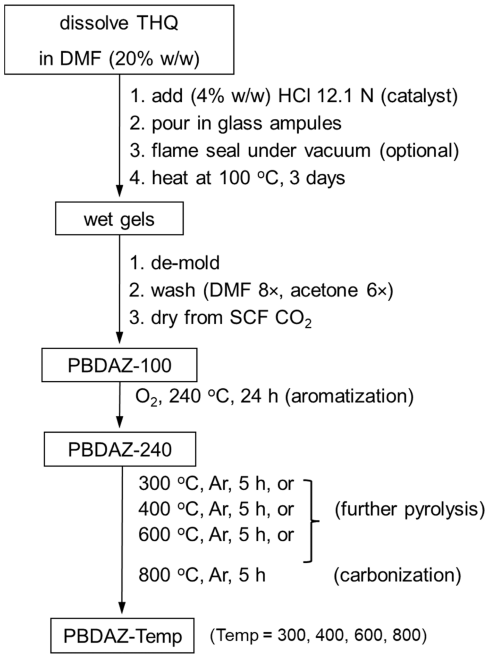


catalyzed with HCl and was carried out at 100 °C. Wet gels were aged in their molds at the gelation temperature for 3 days. Subsequently, the gelation solvent was exchanged with acetone, and wet gels were dried into aerogels with supercritical fluid (SCF) $CO_2$. These as-prepared aerogels are referred to as PBDAZ-100. (All numerical extensions in this article designate processing temperature.) It is noted that owing to clear evidence of autoxidation along the main polymer chain of PBDAZ-100 (see Section 2.2 below), gelation was also carried out in freeze−pump−thaw degassed and flame-sealed tubes. In some experiments, the solvent itself was degassed with Ar prior to its being used to dissolve the monomer. Within the expected variation, aerogels from all processes were chemically and physically identical to one another, leading to the conclusion that oxidation took place post-gelation, either during the solvent-exchange process or even in the dry aerogel form.

*2.1.3. Pyrolysis of PBDAZ Aerogels and the Need For Inserting an Air Oxidation Step.* Figure 1A shows the macroscopic appearance, and Figure 1B shows the corresponding microstructures of a PBDAZ-100 aerogel before and after pyrolysis at 800 °C under flowing Ar. The monolith lost 60% of its mass, got deformed, and the fine dendritic pattern of the as-prepared PBDAZ-100 samples was replaced by a macroporous featureless structure with thick pore walls, in analogy to PBO.[14] Temperature-modulated differential scanning calorimetry (TMDSC) of PBDAZ-100 aerogels under $O_2$ showed a major oxidative event at 205 °C, which was absent when the experiment was run under $N_2$ (Figure 2). Based on these data,

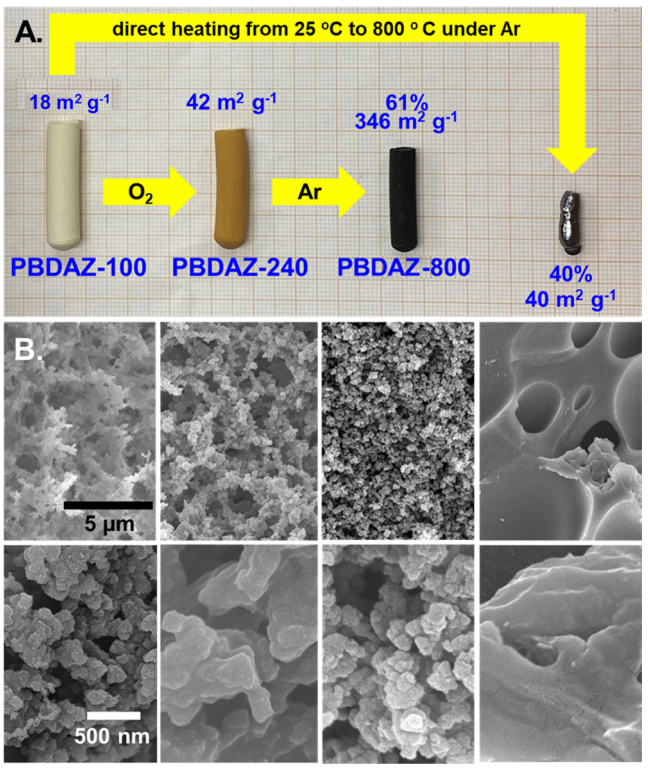


**Figure 1.** (A) Photographs and (B) corresponding SEMs at two different magnifications of typical PBDAZ-100 aerogel samples treated as indicated. (Numerical extensions in the sample names indicate the processing temperatures.)

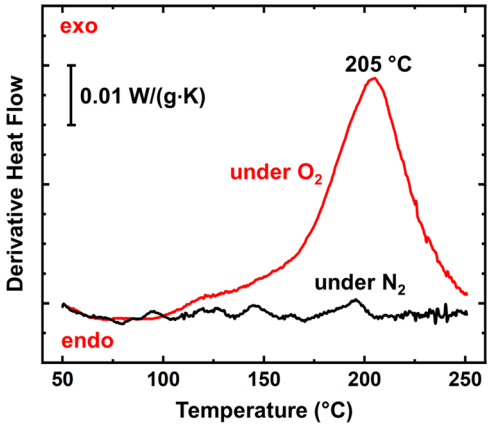


**Figure 2.** Temperature-modulated differential scanning calorimetry (TMDSC) at 5 °C $min^{-1}$ of typical PBDAZ-100 aerogel samples.

PBDAZ-100 aerogels were heated at 240 °C under flowing $O_2$ for 24 h. The resulting aerogels are referred to as PBDAZ-240 (Scheme 3). According to Figure 1A,B, PBDAZ-240 retained approximately the same volume and the fine microstructure of their parent PBDAZ-100 samples, consisting of a random arrangement of fused nanoparticles. Terminal carbonization of PBDAZ-240 was carried out at 800 °C under Ar (Scheme 3). The PBDAZ-800 samples kept their shape and microstructure and lost only about 40% of the mass of their parent PBDAZ-


https://doi.org/10.1021/acs.chemmater.2c02797
Chem. Mater. 2023, 35, 432−446

100. For characterization purposes, several PBDAZ-240 samples were also pyrolyzed at 300, 400, and 600 °C under Ar.

**2.2. Chemical Characterization of THQ along Processing.** The chemical identity of the THQ monomer was investigated spectroscopically. Infrared (IR) spectra, solid-state CPMAS $^{13}$C NMR spectra, and solid-state CPMAS $^{15}$N NMR spectra of THQ and of the aerogels along processing (Scheme 3) are presented in Figures 3−5, respectively. Figure 6 shows the evolution of the CHNO elemental composition from the monomer to the carbon aerogels obtained at 800 °C (Scheme 3).

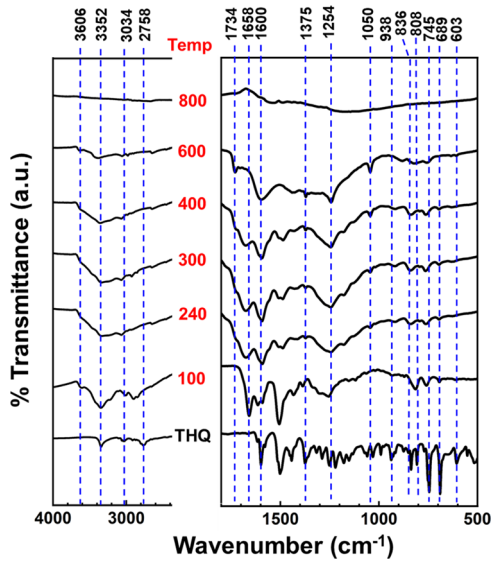


**Figure 3.** Fourier-transform infrared spectra of the benzodiazine monomer (THQ, bottom) and aerogels obtained at different temperatures (Temp) as shown in Scheme 3.

*2.2.1. Chemical Makeup of PBDAZ-100 and PBDAZ-240.* The elucidation of the chemical identity of the PBDAZ-100 and PBDAZ-240 aerogels was complicated by two factors that were not present in the previous case of polybenzoxazine (PBO). First, in the case of PBO, acid-catalyzed polymerization produced stable aerogels. On the contrary, PBDAZ-100 aerogels were prone to autoxidation, which could not be prevented even when gelation and aging were carried out in vacuum-degassed and flame-sealed tubes. Thus, if PBDAZ-100 aerogels were produced via simple ring-opening polymerization, they would have the same chemical composition as the THQ monomer: theoretical % w/w: C, 80.52; H, 6.53; N, 12.95; experimental % w/w: C, 80.62 ± 0.52; H, 6.48 ± 0.27; N, 12.94 ± 0.09. However, the actual composition of PBDAZ-100 included a significant amount of oxygen (% w/w): C, 76.92 ± 0.10; H, 6.20 ± 0.04; N, 11.69 ± 0.06; O, 5.19 ± 0.09. The amount of oxygen was increased further in PBDAZ-240 (% w/w): C, 66.63 ± 0.12; H, 3.10 ± 0.25; N, 11.83 ± 1.50; O, 18.44 ± 1.13. The conclusion was that PBDAZ-100 was always partially oxidized. A second complication stemmed from the polymerization process itself. Referring to Scheme 1, in the case of PBO, initial protonation takes place at the O of the monomer and produces only one kind of an electrophile, a well-defined iminium ion, that was attacked primarily by the available *ortho* position of another monomer, and, to a lesser extent, by the *para* position of a dangling aniline of another monomer.[3,14] Transferring this sequence of events to the polymerization of THQ led to products with features that could not be accounted for by the spectroscopic data. Thereby, our strategy became to consider all possible mechanistic pathways for the $H^+$-catalyzed polymerization of THQ and then select the most probable pathways based on the expected structures that match the experimental spectroscopic data. Thus, according to Scheme 4, THQ offers two sites for initial

**Scheme 4. Summary of All Plausible Reaction Sites in the Benzodiazine Monomer (THQ)**

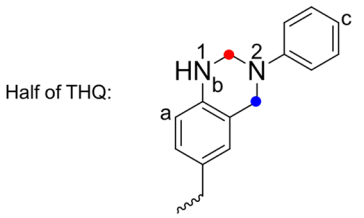


| Protonation at N: | 1 | 2 | |
|---|---|---|---|
| Cation formed at: | ● (red) | ● (red) | ● (blue) |
| Cation attacked by: | a, b or c | a, b or c | a, b or c |

protonation: the two N atoms. Protonation of either N leads to an iminium ion based on the opposite N from the one that was protonated. The two possible iminium ions share a common carbon atom. That common cationic position associated with either iminium ion is marked with a red dot. In addition, protonation of the tertiary aniline N (marked as position 2) may also lead to a benzylic cation at the position marked with a blue dot. Finally, either one of the two cationic positions, the iminium ion or the benzylic cation, may be attacked by three possible nucleophilic sites, a−c, as delineated in Scheme 4. The resulting nine polymerization pathways have been worked out in detail in Appendix I of the Supporting Information. In turn, Appendix II collects from Appendix I and summarizes the structures of all possible polymeric products for both PBDAZ-100, including those from its autoxidation, and PBDAZ-240, including those from full oxidation as well as aromatization.

Referring to Figure 3, below 1000 cm$^{-1}$, the IR of THQ is dominated by (a) a weak yet sharp absorption at 603 cm$^{-1}$ attributed to N−H wagging,[33] (b) a pair of strong absorptions at 689/745 cm$^{-1}$ assigned to the out-of-plane (OOP) C−H bending of the dangling aniline,[34] (c) a pair of weaker absorptions at 808/836 cm$^{-1}$ assigned to the OOP C−H bending of the 1,2,4-trisubstituted aromatic ring,[33] and (d) absorption at 938 cm$^{-1}$, which was attributed to the cyclic aminal of formaldehyde in analogy to the cyclic mixed aminal-acetal of formaldehyde in the BO monomer.[35] The latter absorption was absent from PBDAZ-100, consistent with a ring-opening polymerization process in analogy to benzoxazines.[36] The OOP C−H bending pattern of aniline at 689/745 cm$^{-1}$ became extremely weak after polymerization but was still discernible up to 400 °C. In PBDAZ-100, the 836 cm$^{-1}$ peak of the OOP C−H bending pattern of the 1,2,4-trisubstituted aromatic ring appeared as a shoulder of a new absorption at 814 cm$^{-1}$, while the 808 cm$^{-1}$ peak of the OOP bending pattern of the trisubstituted aromatic ring overlapped and made the new absorption at 814 cm$^{-1}$ look broad. This new absorption at 814 cm$^{-1}$ was the strongest one of PBDAZ-100 below 1000 cm$^{-1}$ and was assigned to the OOP C−H bending of a newly created *para*-substituted aromatic ring.[37] That new ring cannot be based on anything else but the aniline moiety of THQ. Therefore, the major polymerization pathway


https://doi.org/10.1021/acs.chemmater.2c02797
Chem. Mater. 2023, 35, 432−446

engages the *para* position of the dangling aniline of THQ. As far as the 1,2,4-trisubstituted aromatic ring system is concerned, judging from the 808/836 $cm^{-1}$ features, at least some of it survived the polymerization process. Upon further oxidative treatment at 240 °C and beyond, it is noted that in contrast to the dangling aniline pattern that remains discernible, albeit very weak, up to 400 °C, the 814 $cm^{-1}$ absorption of the *para*-substituted aniline ring was already absent from PBDAZ-240, consistent with the premise that polymerization follows at least two distinct pathways and that further oxidation reactions engage the newly formed *para*-substituted aniline.

The 1000−1800 $cm^{-1}$ region of THQ was dominated by the aromatic stretches in the 1400−1600 $cm^{-1}$ region. The absorption at 1375 $cm^{-1}$ with a shoulder at 1354 $cm^{-1}$ was attributed to in-plane $CH_2$ bending.[38] This absorption became very weak in PBDAZ-100, consistent with autoxidation as discussed above, and then even weaker or absent from the spectra of PBDAZ-240 and beyond. The broad absorption in PBDAZ-100 at around 1254 $cm^{-1}$ became better defined in PBDAZ-240 and survived up to 600 °C becoming sharper and dominant. This feature was attributed to aromatic−(C═O)−aromatic stretch like in benzophenone.[33] A second curious absorption band at 1050 $cm^{-1}$ first appeared in PBDAZ-240 and became a dominant feature at 600 °C. This band was attributed to C−O stretching, which was a side effect of ring-fusion aromatization in PBDAZ-240 and beyond (refer to the discussion of the $^{15}N$ NMR spectra below). Next, the new strong peak at 1658 $cm^{-1}$ in the spectrum of PBDAZ-100 was unexpected yet consistent with the C═O stretching of amide and/or urea groups formed via autoxidation of $-CH_2-NH-$ groups like those expected along the backbone of the primary polymerization product, in analogy to polybenzoxazines. Interestingly, this absorption became broader in PBDAZ-240, and its maximum moved to 1675 $cm^{-1}$ and acquired a weak shoulder at 1734 $cm^{-1}$. In analogy to benzophenone (Scheme 5, $\nu_{X=O}$ = 1666 $cm^{-1}$),[39−41] the stretching vibration of

**Scheme 5. Spectroscopic Data for Benzophenone and Fluorenone Relevant to their Carbonyl Groups**

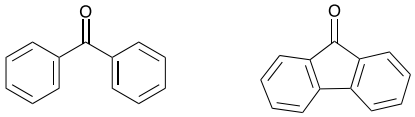


benzophenone

$\nu_{C=O}$(KBr, $cm^{-1}$): 1666 [39]
$\delta_{C=O}$($CDCl_3$, ppm): 196.8 [40]

fluorenone

$\nu_{C=O}$(KBr, $cm^{-1}$): 1715 [39]
$\delta_{C=O}$($CDCl_3$, ppm): 193.7 [41]

benzophenone-like backbone carbonyls created by oxidation of the bridging $CH_2$ groups at the center of the THQ monomer is expected at around 1666 $cm^{-1}$, i.e., partially overlapping with amide and urea carbonyl stretches, hence the observed shift and broadening of the absorption in that region upon oxidation at 240 °C. By 600 °C, the shoulder at 1734 $cm^{-1}$ became a prominent feature and the only surviving carbonyl absorption band in the IR spectrum. Consistently with the eventual carbonization of the PBDAZ aerogels, which involves extensive ring fusion, it is speculated that the band at 1734 $cm^{-1}$ was due to C═O stretching vibration of fluorenone-like moieties (see Scheme 5) formed along the polymeric backbone at high temperatures from the benzophenone-like moieties, in analogy to the catalytic dehydrogenative cyclization of benzophenone to fluorenone.[42]

Finally, looking into the C−H stretching region of THQ, the three absorptions at 2758, 3034, and 3352 $cm^{-1}$ were assigned to the aliphatic C-Hs, the aromatic C-Hs, and the N−H vibrations, respectively. Upon polymerization, the relative intensity of the C−H absorptions in PBDAZ-100 decreased, while the N−H stretching dominated that region, becoming broad, with two shoulders across the maximum. In PBDAZ-240, the aliphatic C−H stretches disappeared, and the aromatic C−H stretches became weak. Beyond 240 °C, the aromatic C−H stretch at 3034 $cm^{-1}$ became even weaker, consistent with ring-fusion aromatization, in analogy to that observed in PBO aerogels.[14] Very weak aromatic C−H stretches were still discernible up to 600 °C. Meanwhile, the broad N−H stretching pattern became weaker but survived up to 400 °C. At 600 °C, the N−H stretch had returned almost to its original intensity as in THQ. Dangling $-NH_2$ groups resulting from polymerization pathways 1-red-a and 1-red-c would have been expected to survive through ring-fusion aromatization at 240 °C and beyond (refer to Schemes S.2 and S.4 of Appendix I in the Supporting Information). Thereby, based on these IR data, pathways 1-red-a and 1-red-c, and the polymers thereof, were considered improbable. Further support for this conclusion was found in the solid-state $^{15}N$ NMR data below.

Peak assignment in the liquid-phase $^{13}C$ NMR spectra of THQ was aided by running experiments in the attached proton test mode (APT, included in Figure 4, bottom left), where resonances corresponding to $CH_2$ carbons and carbons with no hydrogens gave negative peaks. The liquid-phase APT spectrum of THQ was then compared with its solid-state CPMAS $^{13}C$ NMR spectrum. The assignment was further assisted by running all solid-state spectra at two different contact times, 5 $\mu$s and 3000 $\mu$s. If spectra were obtained with 5 $\mu$s contact time (shown in red), carbons bearing no hydrogens disappeared. This is because, in cross-polarization NMR experiments, the build-up of magnetization of each type of $^{13}C$ depends on the dipolar coupling to the protons. As a rule, the closer a $^{13}C$ is to a proton, the faster the magnetization transfer. By reducing the contact time dramatically, only carbons bearing protons are magnetized.

In the solid-state CPMAS $^{13}C$ NMR of PBDAZ-100 (Figure 4, right), the resonance of the bridging central carbon "a" at 40 ppm survived polymerization, but the resonances of the benzylic carbon, h, at 50 ppm, and of the aminal carbon, i, at 60 ppm became extremely weak, consistent with partial autoxidation along the Mannich bridges of the polymeric backbone. On the other hand, no significant aliphatic resonance survived in PBDAZ-240, suggesting quantitative oxidation of all aliphatic carbons, including "a," in agreement with IR. At the same time, a new broad resonance at 192 ppm was assigned to a benzophenone-like carbonyl group formed at that bridging position, "a" (refer to Scheme 5). This new resonance survived subsequent pyrolysis under Ar up to at least the 400−600 °C range. As discussed in conjunction with the IR absorption at 1734 $cm^{-1}$, benzophenone-like C═O is converted to fluorenone-like C═O. While the C═O stretch in fluorenone is expected at a significantly higher frequency than in benzophenone, the $^{13}C$ chemical shift of the two types of carbonyl carbons is about the same (Scheme 5). The dominant resonance in the spectrum of PBDAZ-100 was at 128.4 ppm (versus at 128.9 ppm in THQ), corresponding to the *meta*


https://doi.org/10.1021/acs.chemmater.2c02797
Chem. Mater. 2023, 35, 432−446

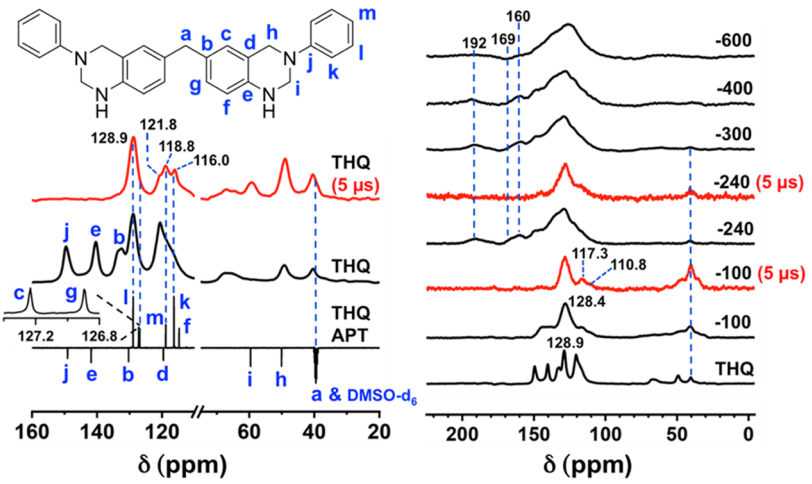


**Figure 4.** Left frame: Bottom, the liquid phase $^{13}C$ attached proton test (APT) spectrum of the benzodiazine monomer (THQ) in DMSO-$d_6$. Middle and top, solid-state CPMAS $^{13}C$ NMR spectra of THQ obtained with contact times equal to 3000 $\mu$s and 5 $\mu$s, respectively. Right frame: Solid-state CPMAS $^{13}C$ NMR spectra of THQ (bottom), PBDAZ-100, PBDAZ-240, and of other aerogels obtained at different pyrolysis temperatures as indicated. All spectra were obtained with contact time = 3000 $\mu$s, except those in red, which were obtained with contact time = 5 $\mu$s.

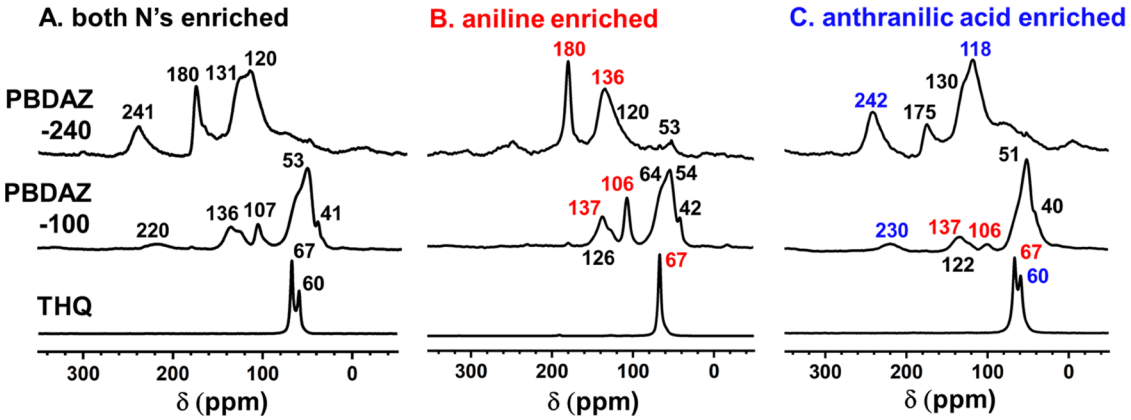


**Figure 5.** Solid-state $^{15}N$ NMR spectra of THQ monomer (bottom), PBDAZ-100 (middle), and PBDAZ-240 (top), using materials selectively enriched with $^{15}N$. Parts A−C as indicated on top.

aniline carbons, l, as well as the carbons at the c and g positions. The lower-intensity peak at 117.3 ppm and its shoulder at 110.8 ppm survived in the 5-$\mu$s spectra and corresponded to the H-bearing *ortho* carbons, k and f, respectively. However, the intensity of f relative to k was decreased compared with THQ, consistent with the conclusion that even if pathways involving the *ortho* position of THQ acting as a nucleophile (i.e., 1-red-a, 2-red-a, 2-blue-a) are still active, their role is minor. (It is also reminded that pathway 1-red-a would also yield dangling $NH_2$ groups that should survive all oxidation and aromatization processes, and thus 1-red-a was eliminated based on both IR and $^{13}C$ NMR grounds.) The *para*-carbon of aniline in THQ, m, was associated with the shoulder at 121.8 ppm. Thus, due to the broadness of the k and f resonances in the solid-state spectra of the aerogels, the fate of the *para*-carbon of aniline, m, was decided exclusively from the IR data, which, as discussed above, clearly showed that m was involved in the primary polymerization/gelation process at 100 °C. Now, apart from the new resonance at 192 ppm, the spectrum of PBDAZ-240 included a broad resonance between 115 and 155 ppm, followed by two new lower-intensity resonances at 160 and 168.8 ppm, which were assigned to urea and amide carbonyls, respectively.[43] The main broad resonance between 115 and 155 ppm was complicated further by several shoulders on either side of its maximum. Nevertheless, when the spectrum of PBDAZ-240 was obtained with contact time = 5 $\mu$s, it was not only simplified relative to the spectrum obtained with contact time = 3000 $\mu$s but above 100 ppm, it also looked practically identical to the spectrum of PBDAZ-100 obtained at 5 $\mu$s. These observations were attributed directly to ring-fusion aromatization, which, in analogy to the corresponding process in polybenzoxazine, caused the loss of protons from certain aromatic C−H positions, thus creating asymmetry that gave rise to complex spectra. However, once newly created tertiary carbons were removed by running the spectra with contact time = 5 $\mu$s, the remaining pattern was similar to the symmetric pattern before oxidative ring-fusion aromatization, i.e., to the spectrum of PBDAZ-100, as expected.

Next, the $^{15}N$ NMR spectrum of THQ (Figure 5A) included only two resonances in the range 60−70 ppm, as expected. Based on $^{1}H$-$^{15}N$ heteronuclear single quantum coherence (HSQC) NMR correlation experiments (see Appendix III in the Supporting Information),[44,45] the resonance at 60 ppm was assigned to the NH nitrogen (coming from anthranilic acid, refer to Scheme 2). Indeed, the $^{15}N$ NMR spectrum of THQ


https://doi.org/10.1021/acs.chemmater.2c02797
Chem. Mater. 2023, 35, 432−446

prepared with $^{15}$N-enriched aniline consisted of only one peak at 67 ppm (Figure 5B). Curiously, however, although selective $^{15}$N enrichment of only the anthranilic acid increased the relative intensity of the corresponding resonance at 60 ppm, the resonance of the nonenriched aniline position at 67 ppm was still more intense than the enriched one (Figure 5C). Initially, this comprised a source of confusion during the interpretation of the solid-state $^{15}$N NMR data of PBDAZ-100 and PBDAZ-240 aerogels, and finally, it was attributed to different spin-lattice relaxation times (T1) of the secondary, NH, versus the tertiary nitrogens. In spite of these difficulties, owing to their relative simplicity over the IR and $^{13}$C NMR data, solid-state $^{15}$N NMR spectra became the main tool for the structure elucidation of PBDAZ-100 and PBDAZ-240. This process was guided by considering all of the polymerization pathways of Scheme 4 (refer to Appendices I and II in the Supporting Information) and the simulated $^{15}$N NMR predictions for all expected products (see Appendix IV in the Supporting Information). Major structural features of the expected products (see Appendix II in the Supporting Information) were cross-checked against the IR and the solid-state $^{13}$C NMR data of Figures 3 and 4.

According to Figure 5, the $^{15}$N NMR spectrum of PBDAZ-100 was dominated by one main resonance at around 51−54 ppm flanked by one low-intensity peak (41 ppm) and a shoulder (64 ppm) on its sides. This pattern was different in PBDAZ-100 obtained by selective enrichment of the one versus the other N in the monomer. Along these lines, and despite the propensity of aniline-derived N to prevail even in the anthranilic acid-enriched monomer, the fact that the spectrum of the PBDAZ-100 derivative of the latter (see Figure 5C) was dominated by a fairly sharp resonance at 51 ppm, indicates that the chemical composition of the PBDAZ-100 aerogels was dominated by just one kind of polymer, in which, importantly, the two types of Ns should be more-or-less in about equivalent positions. The $^{15}$N NMR spectra of PBDAZ-100 also included lower-intensity resonances at around 137 and 106 ppm, consistent with partial autoxidation and formation of amide and urea groups, respectively, along the polymeric backbone, in agreement with the IR and the solid-state $^{13}$C NMR data above. Based on the significantly lower level of O in PBDAZ-100 (5.19% w/w) relative to PBDAZ-240 (18.44% w/w), it is reasonable to assume that partial oxidation causes the conversion of only one (of the two) backbone $-CH_2-$ groups to C═Os per repeat unit. (Oxidation of the bridging $-CH_2-$ in position "a" is not supported by the IR or the $^{13}$C NMR data of PBDAZ-100.) All such singly oxidized forms of PBDAZ-100, irrespective of the pathway, are constitutional isomers (refer to Appendix II in the Supporting Information) with the same expected elemental composition. Considering the experimental composition (% w/w: C, 76.82 ± 0.10; H, 6.23 ± 0.04; N, 11.75 ± 0.06; O, 5.29 ± 0.09) to be the weighted average of the compositions of the as-prepared (%, w/w: C, 80.52; H, 6.52; N, 12.96), and of the two singly oxidized forms (%, w/w: C, 75.63; H, 5.25; N, 12.16; O, 6.96), it was calculated that PBDAZ-100 consisted of 38% w/w of the expected unoxidized polymeric form and 62% w/w of a mixture of the two singly oxidized isomers.

The broad pattern below 100 ppm was no longer present in the spectrum of PBDAZ-240, and this excludes pathways 1-red-a and 1-red-c that would give dangling $-NH_2$ groups originating from the anthranilic acid position. These dangling $-NH_2$ groups would be expected to survive ring-fusion aromatization (refer to Schemes S.2 and S.4 of Appendix I in the Supporting Information). For reasons that will become apparent below, we need to focus our attention on the spectrum of PBDAZ-240 derived from the anthranilic acid-enriched monomer (Figure 5C), which is dominated by a strong resonance at 242 ppm and an even stronger one at 118 ppm (urea). The peak at 242 ppm was not present in PBDAZ-240 from the aniline-enriched monomer. On the other hand, the peak at 118 ppm was present only as a shoulder (at 120 ppm) in PBDAZ-240 from the aniline-enriched monomer. The main resonance with this shoulder was at 136 ppm corresponding to an amide. These observations, taken together with the fact that the $^{15}$N NMR spectra should be dominated by the aniline N, whether enriched or not, mean that the peaks at 242 and 118 ppm come from the main polymeric product, which has its Ns coming from anthranilic acid located either in a very downfield position or in an electron-deficient urea position (i.e., relatively downfield for regular urea). The lower intensity yet prominent resonance at 175 ppm and the amide shoulder (of the urea resonance) at 130 ppm were assigned to the same Ns that appeared at 180 and 135 ppm in the PBDAZ-240 spectrum from the aniline-enriched monomer. For the same reasons that the peak at 67 ppm was stronger than the peak at 60 ppm in the anthranilic acid-enriched spectrum of THQ, if the 242/118 and 175/130 resonances belonged to products from a single pathway, the 175/130 pair would have been more intense than the 242/118 pair. Instead, the fact that the 175/130 pair is less intense than the 242/118 pair points to at least two different pathways being in action. According to Appendix IV in the Supporting Information, pathway 2-blue-c (see Scheme S.10 of Appendix I, summarized here in Scheme 6) yields a fully aromatized form ($F_{Ar}$) with fused aromatic nitrogen coming from anthranilic acid in a more downfield position relative to other possible products—thereby, the

**Scheme 6. PBDAZ-100 and PBDAZ-240 Products from Pathway 2-blue-c[a]**

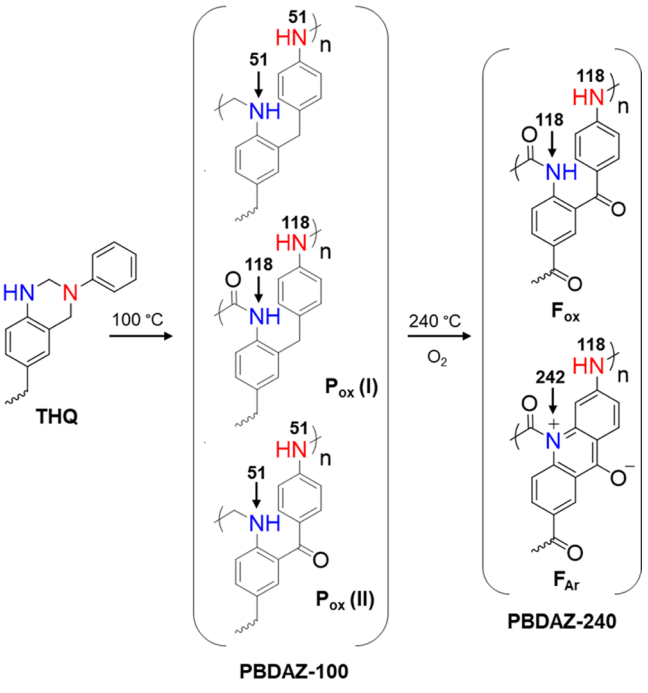


[a]Color-coded N atoms: red, from aniline; blue, from anthranilic acid.


https://doi.org/10.1021/acs.chemmater.2c02797
Chem. Mater. 2023, 35, 432−446

resonance at 242 ppm was assigned to the fused aromatic nitrogen coming from anthranilic acid via pathway 2-blue-c, while the resonance at 118 ppm was assigned to urea-like N coming from aniline. Also, both Ns of the fully oxidized precursor ($F_{OX}$) of the fully aromatized form ($F_{Ar}$) (see Scheme 6) are also classified as ureas and are expected (due to symmetry and the presence of numerous electron withdrawing groups) to appear near the same position as the urea-like nitrogen of $F_{Ar}$ (118 ppm). The presence of both forms, $F_{OX}$ and $F_{Ar}$, provides a reasonable explanation for the fact that the resonance at 118 ppm was more intense than the resonance at 242 ppm. Similarly, again referring to Appendix IV in the Supporting Information, pathways 1-red-b and 2-red-b (for details about these pathways, refer to Schemes S.3 and S.6 of Appendix I) give rise to the amide and urea resonances of PBDAZ-100 at 137 and 106 ppm, respectively, both originating from the aniline nitrogen of THQ and ending up in the two partially oxidized forms (in analogy to $P_{OX}$(I) and $P_{OX}$(II) of the 2-blue-c pathway of Scheme 6). These groups (always traceable to the aniline nitrogen of THQ) evolve into fused pyridinium nitrogens expected at 175−180 ppm (refer to Appendix IV). However, judging from the relative intensities of the 175/130 resonances relative to those at 242/118 ppm and considering the fact that the aniline Ns are always more intense, pathways 1-red-b and 2-red-b shall be minor. Further corroboration about the role of pathways 1-red-b and 2-red-b comes from the fact that neither of these pathways engages the *para* position of the dangling aniline of THQ, consistent with the conclusion from IR data about the presence of concurrent minor polymerization pathways that do not engage the aniline moiety. In spite of all of these analyses, the final point is that the experimental elemental analysis of PBDAZ-240 deviated significantly from the calculated values for $F_{OX}$ and $F_{Ar}$, mostly in terms of carbon and oxygen. For example, PBDAZ-240 contained more oxygen (18.44% w/w) than what is expected from the structures of either the fully oxidized form ($F_{OX}$, 15.92% w/w) or the fully oxidized and aromatized form ($F_{Ar}$, 16.05% w/w). It is speculated that some of the bridging positions "a" in PBDAZ-240 might have been still occupied by the peroxide precursors (C−O−OH) of the carbonyls. For example, the calculated amount of O in $F_{Ar}$ with surviving peroxide is 18.59% w/w. (For the oxidation of PBDAZ-100 to PBDAZ-240, refer to Scheme S.11 of Appendix I in the Supporting Information.)

*2.2.2. Chemical Transformation of PBDAZ-240 toward Carbonization.* Different PBDAZ-240 aerogel samples were pyrolyzed under flowing high-purity argon at 300, 400, 600, or 800 °C (Scheme 3). The resulting samples are referred to as PBDAZ-300, PBDAZ-400, and so on.

According to IR, several functional groups in the bulk of PBDAZ-240 survived up to 600 °C and were identified by their spectroscopic signatures (Figure 3): mainly fluorenone-like carbonyl stretches (1734 $cm^{-1}$), aromatic−(C═O)−aromatic stretches (1254 $cm^{-1}$), C−O stretches (1050 $cm^{-1}$), and isolated fused aromatic group stretches (1600 $cm^{-1}$); no major IR features survived the pyrolysis of PBDAZ-240 at 800 °C. Solid-state $^{13}C$ NMR data corroborated with this picture, the main broad yet well-defined aromatic manifold extending from 115 ppm to 155 ppm that was identified in PBDAZ-240 was also present, practically unchanged, in PBDAZ-600 (Figure 4).

The evolution of the elemental composition as a function of pyrolysis temperature is shown in Figure 6. (For the original data, see Table S.3 of Appendix V in the Supporting Information.) As expected, the percent amount of C and especially of H dropped in PBDAZ-240 compared to the as-prepared PBDAZ-100. On the contrary, the percent amount of O reached 18.44% w/w, significantly higher from 5.19% w/w in PBDAZ-100. Interestingly, the percent amount of N remained practically the same in PBDAZ-240 (11.83% w/w) as in PBDAZ-100 (11.69% w/w). From 240 to 600 °C, we notice a gradual, almost linear increase in the percent amount of carbon (from 67 to 80% w/w) and similar decreases in H (from 3.10 to 2.30% w/w) and O (from 18.44 to 7.83% w/w). Up to 400 °C, the amount of N lingered around its PBDAZ-240 level, followed by a small yet sudden decrease to 10.04% w/w in PBDAZ-600. Between PBDAZ-600 and PBDAZ-800, C increased to 84.29% w/w and H dropped to less than half of its value, to 1.01% w/w. The amount of oxygen remained about constant (at 7.57%), while nitrogen experienced a further drop to 7.13% w/w.

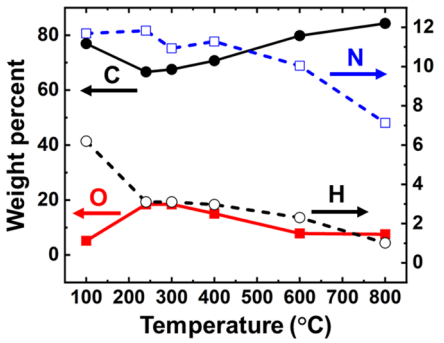


**Figure 6.** Evolution of the elemental composition of polybenzodiazine aerogels along oxidative ring-fusion aromatization and further pyrolytic carbonization.

The chemical makeup of the surfaces of the carbon aerogels obtained by pyrolysis at 800 °C was probed using X-ray photoelectron spectroscopy (XPS). Figure 7 shows the high-resolution O 1s and N 1s XPS spectra of PBDAZ-800. As shown in Figure 7, the two spectra were fitted with two and four Gaussians, respectively. The O 1s spectrum showed two energy levels: one at 532.4 eV, which was assigned to carbonyl oxygen (73.7%),[46] and a second one at 531.4 eV, corresponding to phenoxide $O^-$ (26.3%).[47,48] The N 1s spectrum of PBDAZ-800 showed four energy levels at 398.4 eV (pyridinic N, 26.0%), 400.5 eV (pyridonic N, 57.3%), 401.9 eV (quaternary N, 6.1%), and 403.0 eV (pyridine oxide, 10.6%).[49,50]

Overall, the oxidation of PBDAZ-100 aerogels gave well-defined products (PBDAZ-240) with extensive ring-fusion aromatization along their backbone. Several functional groups introduced during this process survived up to 600 °C in bulk, and their remnants decorated the surfaces of the carbon aerogels received by pyrolysis at 800 °C under an inert atmosphere.

**2.3. Materials Characterization.** Referring to Table 1, the linear shrinkage of PBDAZ-100 aerogels was around 25% relative to the molds. Most of the shrinkage occurred during aging, and no other significant shrinkage was observed during solvent exchange from DMF to acetone and during drying. Oxidation at 240 °C under flowing $O_2$ caused an additional linear shrinkage of 18% in PBDAZ-240 relative to the molds, reaching 36%, which was attributed to the loss of degrees of freedom by aromatization. Post 240 °C, samples shrunk only a little more up to 400 °C, with linear shrinkage reaching 38%.


https://doi.org/10.1021/acs.chemmater.2c02797
Chem. Mater. 2023, 35, 432−446

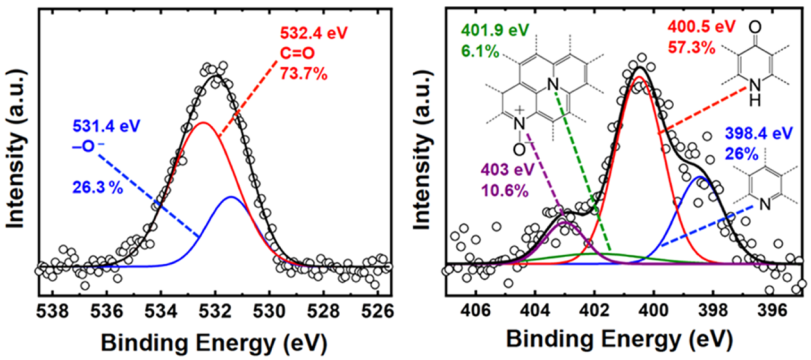


**Figure 7.** High-resolution XPS spectra of O 1s (left) and N 1s (right) in PBDAZ-800.

At 600 °C, shrinkage increased to 42.4%, and at 800 °C, linear shrinkage reached 47%. Overall, shrinkages of the PBDAZ series of samples were similar, both in trend and value, to those reported previously for polybenzoxazine aerogels.[14]

The bulk density ($\rho_b$) of PBDAZ-100 was 0.195 ± 0.008 g cm$^{-3}$. In combination with the sol formulation (20% w/w) and the linear shrinkage, this $\rho_b$ value allows calculation of the mass loss (58.9% w/w) during gelation and further processing. The mass balance of the PBDAZ-100 aerogels relative to the monomer sets the experimentally determined mass loss at 57.77 ± 0.83% w/w. This mass loss is significant yet similar to the mass loss during heat-induced gelation of Ishida's benzoxazine monomer at the same sol concentration but much less than what was reported from the room-temperature HCl-catalyzed preparation of PBO aerogels (only 5−8% w/w).[14] Owing to the combined effect of oxygen uptake and shrinkage, the bulk density of PBDAZ-240 increased to 0.236 ± 0.005 g cm$^{-3}$. Bulk density reached its maximum value at 300 °C (0.258 ± 0.005 g cm$^{-3}$). Afterward, $\rho_b$ decreased gradually, reaching 0.225 ± 0.001 g cm$^{-3}$ at 800 °C, reflecting the relative interplay of pyrolytic mass loss and shrinkage. By comparison, the reported bulk densities of carbon aerogels derived from polybenzoxazine aerogels pyrolyzed at 800 °C were in the range of 0.46−0.89 g cm$^{-3}$.[14] The overall trends in bulk densities of both PBO and PBDAZ-derived carbon aerogels reflect the initial densities of their parent polymeric aerogels.

The skeletal density ($\rho_s$) of the as-prepared PBDAZ-100 was 1.575 ± 0.003 g cm$^{-3}$ and decreased to 1.442 ± 0.009 g cm$^{-3}$ in PBDAZ-240. The value of $\rho_s$ decreased further up to 400 °C and then started to increase at 600 °C. $\rho_s$ was almost back to the level of the as-prepared samples, reaching graphite-like values (2.20 g cm$^{-3}$) at 800 °C.

The open porosity, Π, calculated as the percent empty space via $\Pi = 100 \times (\rho_s - \rho_b)/\rho_s$, varied from 88% v/v in PBDAZ-100 to 84% v/v in PBDAZ-240. Eventually, the porosity of PBDAZ-800 reached 90%, signifying the higher contribution of the pyrolytic mass loss in creating empty space relative to the contribution of the volumetric shrinkage in limiting that space as pyrolysis temperature was increased. These properties were utilized recently to prepare carbon aerogels from xerogel powders.[20]

Referring back to Figure 1, microscopically, PBDAZ-100 comprised a dendritic structure, which at higher magnifications consisted of clusters of fused particles. PBDAZ-240 consisted of string-like arrangements of particles, which, at higher magnifications, again seemed to consist of fused clusters of particles. Qualitatively, the sizes of individual particles in the fused clusters of PBDAZ-240 appeared somewhat larger than the particles in PBDAZ-100. Both PBDAZ-100 and PBDAZ-240 aerogels included micron-size voids (macropores). The microscopic appearance changed drastically upon pyrolysis at 800 °C. On average, the pore size decreased, large macropores were no longer present, while the particles, at least at low magnification, looked finer (refer to Figure 1B). Quantitative information about both particle sizes and the pore structure was obtained with $N_2$ sorption porosimetry at 77 K (Figure 8).

The $N_2$-sorption isotherms of PBDAZ-100 and PBDAZ-240 (Figure 8A) showed narrow hysteresis loops without saturation plateaus, indicating mostly macroporous materials in agreement with SEM (Figure 1). The shape of the isotherms at the high-pressure end (i.e., as the partial pressure approached unity ($P/P_o \rightarrow 1$)) did not change with increasing pyrolysis temperature (Figure 8B). However, the low-pressure end of the isotherms of the PBDAZ-600 and PBDAZ-800 aerogels was dominated by a sharp early rise, indicating the presence of microporosity. This behavior is quite analogous to that of polybenzoxazine aerogels, and if it is considered together with the results from the direct pyrolysis of PBDAZ-100 at 800 °C (i.e., without the 240 °C-curing step in air, see Figure 1), it is concluded that microporosity was created not as a result of some sort of inherent molecular rigidity in PBDAZ-100 (in the context of intrinsically microporous polymers[51]), but rather as a result of the rigidity imposed by the ring-fusion aromatization step at 240 °C/air.[14]

The BET surface area, $\sigma$, of PBDAZ-100 and PBDAZ-240 was low ($\sigma$ = 18 and 42 m$^2$ g$^{-1}$, respectively) and remained in the same range up to PBDAZ-400. Based on t-plot analysis with the Harkins and Jura method,[52] a small percentage (<20%) of this BET surface area was attributed to micropores (Table 1). The BET surface area increased dramatically in PBDAZ-600 and PBDAZ-800, reaching 432 and 346 m$^2$ g$^{-1}$, respectively. Consistent with the sharp rise of the isotherms of those two samples at $P/P_o \ll 0.1$, a large part of their BET surface areas (79% in both materials) was attributed to micropores (Table 1). Average particle radii, $r$, were calculated from skeletal density and surface area data via the expression $r = 3/(\rho_s \times$ external surface area), where external surface area = BET surface area ($\sigma$) − micropore surface area. All relevant data are summarized in Table 1. Despite the fact that in SEM the fused skeletal particles in PBDAZ-240 appeared slightly larger than the skeletal particles in PBDAZ- 100, the calculated average skeletal particle radius in PBDAZ-240 was actually about half of the skeletal particle radius in PBDAZ-100 (56 versus 127 nm, respectively), a fact attributed to better-defined inter-particle necking. A further reduction in the skeletal


https://doi.org/10.1021/acs.chemmater.2c02797
Chem. Mater. 2023, 35, 432−446

Table 1. General Material Properties of PBDAZ Aerogels and the Derived Carbons (Refer to Scheme 3)

| sample | linear shrinkage [%][a,b] | bulk density, $\rho_b$ [g cm$^{-3}$][a] | skeletal density, $\rho_s$ [g cm$^{-3}$][c] | porosity, $\Pi$ [% v/v][d] | specific pore volume [cm$^3$ g$^{-1}$] | | | | surface area BET, $\sigma$ (micropore)[i] [m$^2$ g$^{-1}$] | pore diameter via $4 \times V/\sigma$ [nm][j] | micropore diameter [nm][k] | particle radii via $3/(\rho_s \times s)$ [nm][l] |
|---|---|---|---|---|---|---|---|---|---|---|---|---|
| | | | | | $V_{total}$[e] | $V_{1.7-300nm}$[f] | $V_{max}$[g] | $V_{micropore}$[h] | | | | |
| PBDAZ-100 | 25.1 ± 2 | 0.195 ± 0.008 | 1.575 ± 0.003 | 88 | 4.50 | 0.03 | 0.03 | | 18 (3) | 998 (6.6) | | 127 |
| PBDAZ-240 | 35.7 ± 0.07 | 0.236 ± 0.005 | 1.442 ± 0.009 | 84 | 3.54 | 0.03 | 0.10 | | 42 (4) | 338 (9.5) | | 55 |
| PBDAZ-300 | 36.2 ± 0.3 | 0.258 ± 0.005 | 1.369 ± 0.013 | 81 | 3.14 | 0.04 | 0.05 | | 23 (3) | 547 (8.7) | | 110 |
| PBDAZ-400 | 37.6 ± 0.2 | 0.231 ± 0.002 | 1.394 ± 0.007 | 83 | 3.60 | 0.05 | 0.07 | | 37 (8) | 390 (7.6) | | 74 |
| PBDAZ-600 | 42.4 ± 0.2 | 0.216 ± 0.005 | 1.546 ± 0.012 | 86 | 3.98 | 0.06 | 0.27 | 0.18 | 432 (342) | 37 (2.5) | 0.564 | 22 |
| PBDAZ-800 | 46.8 ± 0.1 | 0.225 ± 0.001 | 2.197 ± 0.018 | 90 | 3.99 | 0.05 | 0.19 | 0.15 | 346 (274) | 46 (3.0) | 0.561 | 19 |

[a]Average of five samples. [b]All values relative to molds. [c]Single sample, an average of 50 measurements. [d]Via $\Pi = 100 \times (\rho_s - \rho_b)/\rho_s$, [e]$V_{total} = (1/\rho_b) - (1/\rho_s)$. [f]BJH-desorption cumulative pore volume. [g]$V_{max}$: single point $N_2$ adsorption at 77 K as $P/P_0 \rightarrow 1.0$. [h]Cumulative volume of $N_2$-adsorbed at $P/P_0 \leq 0.1$ using the Horvath−Kawazoe method applied to $N_2$-sorption data under low-pressure dosing and assuming micropores with cylindrical geometry. [i]BET surface areas: before the parentheses. Micropore surface areas (in parentheses) were calculated using $t$-plot analysis with the Harkins and Jura method. [j]For the first values before the parentheses, $V = V_{total}$; for the values (in parentheses), $V = V_{max}$; for $V_{total}$ and $V_{max}$, refer to footnotes e and g. [k]Median pore diameter obtained with the Horvath−Kawazoe method applied to $N_2$-sorption data under low-pressure dosing and assuming pores with cylindrical geometry. [l]External surface area ($s$) = BET surface area ($\sigma$) − micropore surface area.

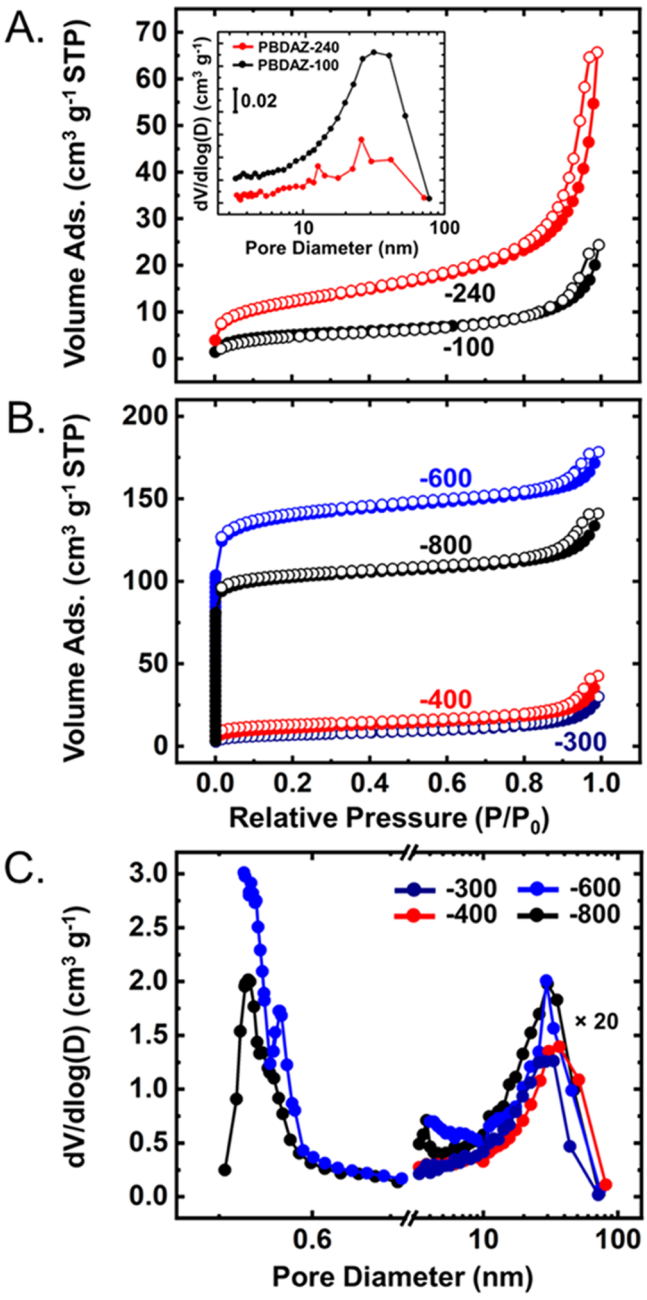


**Figure 8.** (A, B) $N_2$-sorption isotherms at 77 K of PBDAZ aerogel samples obtained at the temperatures shown as labels of the corresponding isotherms. The inset in part A: the BJH pore-size distribution of the corresponding samples. (C) Comparison of the BJH pore-size distributions of the samples in Part B and the micropores in PBDAZ-600 and PBDAZ-800.

particle size was noted in PBDAZ-600 and PBDAZ-800 (21 and 19 nm, respectively).

The specific pore volumes of pores with sizes in the range of 1.7−300 nm, $V_{1.7-300nm}$, were calculated from the $N_2$ sorption data with the BJH method.[53] In line with the large (>300 nm) macropores observed in SEM, $V_{1.7-300nm}$ for all samples were found to be significantly smaller than the corresponding total specific pore volumes, $V_{total}$, calculated via $V_{total} = (1/\rho_b) - (1/\rho_s)$. Now, the fact that for PBDAZ-600 and PBDAZ-800, the values of $V_{max}$, the specific pore volumes registered as $P/P_o \rightarrow 1$, were 4−5 times larger than the corresponding $V_{1.7-300nm}$ corroborates with the presence of more pores with sizes less


https://doi.org/10.1021/acs.chemmater.2c02797
Chem. Mater. 2023, 35, 432−446

than 1.7 nm (i.e., micropores) than mesopores. This is not noticed frequently with the as-prepared carbon aerogels. However, it has indeed been observed before with thermally polymerized polybenzoxazines at the same sol concentration as in this report (20% w/w).[14] Micropore volumes, $V_{micropore}$, were calculated using the Horvath−Kawazoe method applied on the low-pressure part of the isotherms of PBDAZ-600 and PBDAZ-800 (see Table 1).[54] Indeed, $V_{micropore} \gg V_{1.7-300nm}$, but the sum of $V_{micropore} + V_{1.7-300nm} \approx V_{max}$. Interestingly, the $V_{micropore}$ of PBDAZ-600 (0.18 $cm^3\ g^{-1}$) was higher than the $V_{micropore}$ of PBDAZ-800 (0.15 $cm^3\ g^{-1}$).

Using the $4 \times V/\sigma$ method, pore volumes can be used to calculate average pore diameters. Thus, by setting $V = V_{total}$, the average pore diameters were found in the 300 nm to 1 $\mu$m range for all samples up to PBDAZ-400, consistent with the macroporosity observed in SEM. The average pore diameters dropped to 37 and 46 nm in PBDAZ-600 and PBDAZ-800, respectively, consistent with increasing $V_{max}$. By setting $V = V_{max}$, the average pore diameters of the aerogel samples up to PBDAZ-400 fell in the low mesopore range (7−10 nm). Then, reflecting the presence of significant microporosity in PBDAZ-600 and PBDAZ-800, the average pore diameters calculated via $4 \times V_{max}/\sigma$ decreased to 2−3 nm. Irrespective of the presence of macroporosity or microporosity, the pore-size distributions by the BJH-desorption method of the small amount of pores within the mesopore range were practically identical in all samples, all with maxima at around 20−30 nm (Figure 8A,C). The average pore sizes of the micropores in PBDAZ-600 and PBDAZ-800 were calculated from the micropore size distributions (see Figure 8C), which in turn were obtained using the Horvath−Kawazoe method applied on the $N_2$-sorption data at $P/P_o \ll 1$ assuming pores with cylindrical geometry. Although the median pore sizes were similar for the two materials (0.564 and 0.561 nm, for PBDAZ-600 and PBDAZ-800, respectively), the corresponding pore-size distributions were different, consistent with further molecular rearrangement and change in chemical composition by pyrolysis at a higher temperature.

## 3. CONCLUSIONS

Highly porous monolithic polybenzodiazine aerogels were synthesized via ring-opening polymerization of an all-nitrogen analogue of Ishida's benzoxazine monomer. In contrast to polybenzoxazines, however, the formation of polybenzodiazine can take any of several parallel pathways leading to a more complicated molecular structure. Yet, in analogy to polybenzoxazines, high-yield pyrolytic carbonization requires prior oxidative ring-fusion aromatization of the as-prepared polymeric backbone, which was carried out at 240 °C under a stream of $O_2$. Carbon aerogels derived from aromatized polybenzodiazine aerogels had high microporous surface areas and contained 10.04% w/w of N after pyrolysis at 600 °C and 7.13% w/w of N after pyrolysis at 800 °C. By comparison, structurally analogous polybenzoxazine-derived carbon aerogels obtained at 800 °C contain 5.24% w/w N. Thereby, carbon aerogels derived from the structurally analogous polybenzodiazine/polybenzoxazine pair comprise a sufficient basis for exploring the importance of nitrogen doping for adsorption (e.g., of $CO_2$), which is going to be the subject of a subsequent publication.

## 4. EXPERIMENTAL SECTION

**4.1. Materials.** All reagents and solvents were used as received, unless noted otherwise. Anthranilic acid, formaldehyde, aniline, triethyl orthoformate, aluminum chloride, lithium aluminum hydride, and tetrahydrofuran (THF) were obtained from Sigma-Aldrich Co. $^{15}$N-enriched anthranilic acid and $^{15}$N-enriched aniline were purchased from Cambridge Isotope Limited. Dimethylformamide (DMF), concentrated hydrochloric acid (HCl), triphosgene, dioxane, ethanol, methanol, and acetone were obtained from Fischer Scientific International, Inc. Siphon grade $CO_2$, argon (99.999%), and $N_2$ (99.999%) were purchased from Ozark Gas (Rolla, MO). Liquid $N_2$ and $O_2$ gas (99.999%) were purchased from Air Gas (St. Louis, MO). A propane hand torch cylinder (87.5−100%) was purchased from BernzOmatic (Newark, NJ).

*4.1.1. Synthesis of 5,5′-Methylenebis(2-aminobenzoic acid) (Also Referred to as 4,4′-Methylenebis Anthranilic Acid, Intermediate 2, Scheme 2).*

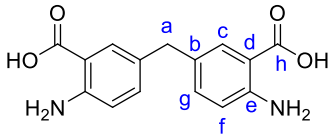


A 3% aqueous formaldehyde solution (140 mL) was added to a magnetically stirred solution of anthranilic acid **1** (27.4 g, 200 mmol) in $H_2O$ (500 mL) containing concentrated HCl (36%, 100 mL) in a round-bottom flask kept at 50 °C in an oil bath. The resulting solution was heated to 70 °C under stirring for 4 h. At the end of the period, the solution was allowed to cool down to room temperature and was neutralized (to pH 7) with concentrated aqueous ammonium hydroxide. The precipitate was collected, washed with hot $H_2O$, and air-dried on the filter for 16 h. Received: 45.5 g of **2** as a yellow solid (Yield = 79.5%). Mp: 258−260 °C. $^1$H NMR (400 MHz, DMSO-$d_6$—refer to Appendix VI in the Supporting Information): $\delta$ (ppm) 8.50 (bs, 4H, $NH_2$), 7.47 (s, 2H, $H_c$), 7.04 (d, $J$ = 8.4 Hz, 2H, $H_g$), 6.67 (d, $J$ = 8.4 Hz, 2H, $H_f$), 3.60 (s, 2H, $H_a$). $^{13}$C NMR (100 MHz, DMSO-$d_6$): $\delta$ (ppm) 169.5 (s, 2C, $C_h$), 149.7 (s, 2C, $C_e$), 134.4 (s, 2C, $C_g$), 130.5 (s, 2C, $C_c$), 127.7 (s, 2C, $C_b$), 116.6 (s, 2C, $C_f$), 109.4 (s, 2C, $C_d$), 39.0 (s, 1C, $C_a$). ATR-FTIR ($cm^{-1}$): 3472 and 3370 ($NH_2$ stretching), 3071 (OH stretching), 2923, 1664 (C═O stretching), 1584, 1557, 1490, 1409, 1297, 1229, 1204, 1165, 1102, 892, 837, 675. Elemental analysis (% w/w), calculated for $C_{15}H_{14}N_2O_4$: C, 62.93; H, 4.93; N, 9.79; O, 22.35. Found: C, 62.04; H, 4.88; N, 9.82; O, 23.26.

*4.1.2. Synthesis of 6,6′-Methylenebis(1H-benzo[d][1,3]oxazine-2,4-dione) (Intermediate 3, Scheme 2).*

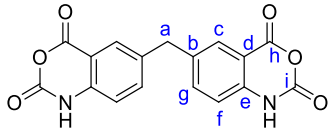


A mixture of intermediate **2** (28.6 g, 100 mmol) and triphosgene (19.5 g, 66 mmol) was refluxed in dioxane (400 mL) for 6 h. The precipitate was collected, washed with hot dioxane, and dried in a vacuum oven at 80 °C for 12 h. Received: 32.2 g of **3** as a white solid (Yield = 95.2). Mp: 260 °C (dec.). $^1$H NMR (400 MHz, DMSO-$d_6$—refer to Appendix VI in the Supporting Information): $\delta$ (ppm) 11.6 (s, 2H, NH), 7.80 (s, 2H, $H_c$), 7.65 (d, $J$ = 8.4 Hz, 2H, $H_g$), 7.10 (d, $J$ = 8.4 Hz, 2H, $H_f$), 4.04 (s, 2H, $H_a$). $^{13}$C NMR (100 MHz, DMSO-$d_6$): $\delta$ (ppm) 160.0 (s, 2C, $C_h$), 147.1 (s, 2C, $C_i$), 139.9 (s, 2C, $C_e$), 137.6 (s, 2C, $C_b$), 136.4 (s, 2C, $C_g$), 128.4 (s, 2C, $C_c$), 115.7 (s, 2C, $C_f$), 110.4 (s, 2C, $C_d$), 38.7 (s, 1C, $C_a$). ATR-FTIR ($cm^{-1}$): 3176 (NH stretching), 3087, 2980, 2927, 1776 (C═O stretching), 1731 (C═O stretching), 1625, 1514, 1431, 1338, 1271, 1255, 1112, 1080, 1032, 985, 861, 746. Elemental analysis (% w/w), calculated for $C_{17}H_{10}N_2O_6$: C, 60.36; H, 2.98; N, 8.28; O, 28.38. Found: C, 60.40; H, 2.94; N, 8.32; O, 28.34.


https://doi.org/10.1021/acs.chemmater.2c02797
Chem. Mater. 2023, 35, 432−446

*4.1.3. Synthesis of 6,6′-Methylenebis(3-phenylquinazolin-4(3H)-one) (Intermediate 4, Scheme 2).*

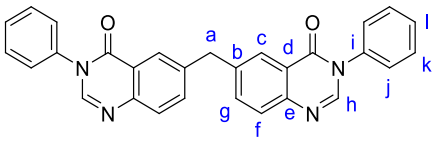

Aniline (27.9 g, 300 mmol) was added to the mixture of intermediate **3** (33.8, 100 mmol) and triethyl orthoformate (44.4 g, 300 mmol) in ethanol (500 mL). The resulting mixture was stirred magnetically at 80 °C for 18 h. At the end of the period, the mixture was cooled back to room temperature, and the precipitate was collected, washed with ethanol, and air-dried in a vacuum oven at 80 °C for 12 h. Received: 30.6 g of **4** as a white solid (Yield = 66.9%). Mp: 208−210 °C. $^1$H NMR (400 MHz, $CDCl_3$—refer to Appendix VI in the Supporting Information): $\delta$ (ppm) 8.19 (s, 2H, $H_h$), 8.07 (s, 2H, $H_c$), 7.70 (d, $J$ = 8.4 Hz, 2H, $H_g$), 7.62 (d, $J$ = 8.4 Hz, 2H, $H_f$), 7.52 (t, $J$ = 7.2, 4H, $H_k$), 7.46 (t, $J$ = 7.2, 2H, $H_l$), 7.40 (d, $J$ = 7.2, 4H, $H_j$), 4.27 (s, 2H, $H_a$). $^{13}$C NMR (100 MHz, $CDCl_3$): $\delta$ (ppm) 161.1 (s, 2C, C═O), 147.1 (s, 2C, $C_h$), 146.3 (s, 2C, $C_e$), 140.6 (s, 2C, $C_i$), 138.0 (s, 2C, $C_b$) 136.1 (s, 2C, $C_g$), 130.1 (s, 4C, $C_k$), 129.6 (s, 2C, $C_c$), 128.5 (s, 4C, $C_l$), 127.5 (s, 2C, $C_j$), 127.3 (s, 2C, $C_f$), 122.9 (s, 2C, $C_d$), 41.9 (s, 1C, $C_a$). ATR-FTIR (cm$^{-1}$): 3053, 3033, 1773, 1698 (C═O stretching), 1593, 1484, 1453, 1336, 1260, 1025, 986, 748. Elemental analysis (% w/w), calculated for $C_{29}H_{20}N_4O_2$: C, 76.30; H, 4.42; N, 12.27 O, 7.01. Found: C, 76.22 H, 4.40; N, 12.22; O, 7.16.

*4.1.4. Synthesis of Bis(3-phenyl-1,2,3,4-tetrahydroquinazolin-6-yl)methane (THQ, Schemes 1 and 2).*

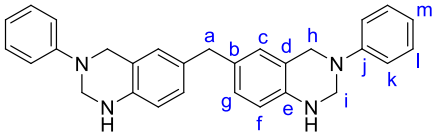

A solution of anhydrous aluminum chloride (10.6 g, 80 mmol) in THF (320 mL) was added to a suspension of lithium aluminum hydride (4.56 g, 120 mmol) in THF (280 mL), and the mixture was stirred at 0 °C for 1 h. Intermediate **4** (18.2 g, 40 mmol) was added as a solid to the cold solution, and the mixture was stirred for 2 h at 0 °C. At the end of this period, stirring was stopped and crushed ice was added to the mixture. The solids were filtered off and washed with cold THF. The mother liquid and the THF washes were combined. The solvent was removed under reduced pressure with a rotary evaporator to afford the crude product as a yellow solid (14.6 g, 84%). Subsequently, the crude product was refluxed for 2 h in 230 mL of methanol in a round-bottom flask. The solid was filtered hot and washed with hot methanol. Received: 7.5 g of THQ as a white solid (Yield = 43%). Mp: 150−153 °C. $^1$H NMR (400 MHz, DMSO-$d_6$—refer to Appendix VI in the Supporting Information): $\delta$ (ppm) 7.20 (m, 4H, $H_l$), 7.02 (d, $J$ = 8.2 Hz, 4H, $H_k$), 6.78 (m, 6H, $H_c$, $H_g$, $H_m$) 6.42 (d, $J$ = 8.2 Hz, 2H, $H_f$), 5.82 (t, $J$ = 3.5, 2H, NH), 4.60 (d, $J$ = 3.5 Hz, 4H, $H_i$), 4.41 (s, 4H, $H_h$), 3.58 (s, 2H, $H_a$). $^{13}$C NMR (100 MHz, DMSO-$d_6$): $\delta$ (ppm) 149.0 (s, 2C, $C_j$), 141.8 (s, 2C, $C_e$), 130.3 (s, 2C, $C_b$), 128.9 (s, 4C, $C_l$), 127.2 (s, 2C, $C_c$), 126.8 (s, 2C, $C_g$), 119.6 (s, 2C, $C_d$), 118.8 (s, 2C, $C_m$), 116.3 (s, 4C, $C_k$), 114.7 (s, 2C, $C_f$), 59.6 (s, 2C, $C_i$), 50.1(s, 2C, $C_h$), 39.9 (s, 1C, $C_a$). $^{15}$N NMR (40.557 MHz, DMF-$d_7$): $\delta$ (ppm) 60.09. Solid-state $^{15}$N NMR (40.557 MHz; magic angle spinning 5 kHz): $\delta$ (ppm) 67.13, 59.48. ATR-FTIR (cm$^{-1}$): 3252 (NH stretching), 3014, 2888, 2830, 1596 (C-C stretching), 1491 (trisubstituted benzene stretching), 1298 (C-N stretching),1248, 1219, 1125, 1028, 992, 926, 825, 745, 689. Elemental analysis (% w/w), calculated for $C_{29}H_{28}N_4$: C, 80.52; H, 6.53; N, 12.95. Found: C, 80.62 ± 0.52; H, 6.48 ± 0.27; N, 12.94 ± 0.09.

*4.1.5. Preparation of Polybenzodiazine Aerogels (PBDAZ-100).* In a typical process, THQ monomer (10 g) was dissolved in 38 g of DMF. Concentrated aq. HCl (12.1 N, 2 g) was added to this solution to obtain the sol. The weight percent concentration of the THQ monomer in the sol was 20% w/w. The sol was stirred at room temperature for 10 min, and then it was syringed into molds. The molds could be prior flame elongated Pyrex tubes (1 cm in diameter x 10 cm in length). Each tube was purged with argon for 1 min and subsequently was degassed with three freeze−pump−thaw cycles at 77 K. At the end of the third cycle, and while tubes remained submerged in liquid nitrogen, they were flame-sealed under vacuum using a propane hand-held torch (BernzOmatic, TS3500K). The sol inside the vacuum-sealed tubes was left for gelation at 100 °C for 3 days. At the end of this period, the tubes were broken open, the gels were removed, and washed with DMF (8×, 4 h each time) and acetone (6×, 4 h each time). The amount of solvent used for each wash was 4× the volume of the gel. Finally, wet gels were dried in an autoclave with liquid $CO_2$ taken out at the end as a supercritical fluid. The resulting aerogels are referred to as PBDAZ-100.

*4.1.6. Oxidative Aromatization of PBDAZ-100 to PBDAZ-240.* PBDAZ-100 aerogel monoliths were transferred to a tube furnace. The temperature of the furnace was raised to 240 °C at 2.5 °C min$^{-1}$ under flowing $O_2$ (0.3 L min$^{-1}$) and remained under these conditions for 24 h. The resulting aerogels are referred to as PBDAZ-240.

*4.1.7. Synthesis of $^{15}$N-Enriched THQ, PBDAZ-100, and PBDAZ-240.* During the synthesis of THQ (Sections 4.1.2−4.1.4), a mixture of $^{15}$N-enriched and regular unlabeled anthranilic acid (containing 10% mol:mol of the enriched compound) was used to obtain THQ with only its secondary nitrogen position enriched with $^{15}$N. Separately, a mixture of $^{15}$N-enriched and regular unlabeled aniline (also containing 10% mol:mol of the enriched compound) was used to obtain THQ with only its tertiary nitrogen position enriched with $^{15}$N. Also, THQ with both nitrogen positions enriched with $^{15}$N (in a 1:1 mole ratio) was obtained using similar 10% mol:mol mixtures of $^{15}$N-enriched anthranilic acid and $^{15}$N-enriched aniline at the respective steps of the synthesis. The three different versions of $^{15}$N-enriched THQ were used to make PBDAZ-100 aerogels as described in Section 4.1.5, and the latter were aromatized to PBDAZ-240 as described in Section 4.1.6

*4.1.8. Pyrolytic Conversion of PBDAZ-240 Aerogels to Carbon Aerogels (PBDAZ-600 and PBDAZ-800).* PBDAZ-240 aerogel monoliths were placed in the tube furnace under flowing argon (0.3 L min$^{-1}$) and were heated (2.5 °C min$^{-1}$) either at 600 °C or at 800 °C for 5 h. The resulting aerogels are referred to as PBDAZ-600 or PBDAZ-800, respectively. For monitoring the process along pyrolysis, several PBDAZ-240 aerogel monoliths were heated under flowing argon for 5 h at 300, 400, and 600 °C. Separate PBDAZ-240 samples were used for pyrolysis at each temperature. After treatment at each pyrolysis temperature, the corresponding samples were returned to room temperature and characterized.

**4.2. Methods.** *4.2.1. Drying Wet Gels into Aerogels.* Drying wet gels into aerogels was carried out in an autoclave (SPI-DRY Jumbo Supercritical Point Dryer, SPI Supplies, Inc. West Chester, PA). Samples were placed in the special boat supplied with the autoclave, and acetone was added until the samples were submerged. The boat was loaded into the autoclave that was kept at 14 °C. The pressure vessel was closed, and liquid $CO_2$ was allowed in multiple times, and each time it was drained out through a valve at the bottom of the autoclave. The cycle was repeated until all of the acetone was extracted out of the pores of the samples completely. The end-of-process criterion was that $CO_2$ released through the drain valve formed dry ice. Subsequently, the temperature of the autoclave was raised to 40 °C. After a stay at that temperature for 1 h, supercritical fluid (SCF) $CO_2$ was vented off as a gas over a period of 5 h.

*4.2.2. Pyrolysis and Carbonization.* All pyrolytic processes were conducted in a tube furnace (MTI GSL1600X-80). The heating rate was always 2.5 °C min$^{-1}$, and the gas (argon or oxygen) flow rate was always set at 0.3 L min$^{-1}$.

*4.2.3. Physical Characterization.* Bulk densities ($\rho_b$) were calculated from the weight and the physical dimensions of the samples. Skeletal densities ($\rho_s$) were measured using helium pycnometry with a Micromeritics AccuPyc II 1340 instrument.

*4.2.4. Chemical Characterization.* CHN elemental analysis was conducted with an Exeter Analytical Model CE440 elemental analyzer calibrated with acetanilide, urea, and glycine. The combustion furnace


https://doi.org/10.1021/acs.chemmater.2c02797
Chem. Mater. 2023, 35, 432−446

was operated at 1050 °C. All of the calibration standards and samples were run three times, and the results are given as averages.

Attenuated total reflectance infrared spectra (ATR-IR) were obtained with a Nicolet FTIR Model iS50 spectrophotometer.

Liquid NMR spectra, including $^{13}$C APT (attached proton test), were recorded with a 400 MHz Varian Unity Inova NMR instrument (100 MHz and 40.557 MHz carbon and nitrogen frequencies, respectively). A $^{1}$H-$^{15}$N heteronuclear single quantum coherence (HSQC) NMR spectrum was recorded on the same spectrometer [400 MHz($^{1}$H), 40.557 MHz($^{15}$N)]. Solid-state CP TOSS $^{13}$C NMR spectra were obtained from samples ground into fine powders on a Bruker Avance III 400 MHz spectrometer with a carbon frequency equal to 100 MHz, using a 7 mm Bruker MAS probe at a magic angle spinning rate of 5 kHz, with broadband proton suppression and CP TOSS pulse sequence for the total suppression of side spinning bands. Solid-state $^{13}$C NMR spectra were referenced externally to glycine (carbonyl carbon at 176.03 ppm). Chemical shifts are reported versus TMS (0 ppm). Solid-state CPMAS $^{15}$N NMR spectra were obtained on the same Bruker Avance III 400 MHz spectrometer with a nitrogen frequency of 40.557 MHz, using a 7 mm Bruker MAS probe and magic angle spinning at 5 kHz, with broadband proton suppression. Chemical shifts are reported versus liquid ammonia (0 ppm) and were externally referenced to glycine (amine nitrogen at 33.40 ppm versus liquid ammonia). In all of the $^{13}$C and $^{15}$N solid-state NMR experiments, the relaxation delay was set at 5 s. In selected $^{13}$C solid-state NMR experiments, the results were compared at two different contact times (P15): 5 $\mu$s and 3000 $\mu$s. Simulated $^{15}$N NMR predictions for all expected products (see Appendix IV in the Supporting Information) were obtained using the ACD/Spectrus Processor 2020, Version 1.2 software package distributed from Advanced Chemistry Development, Inc. (Toronto, CA).

X-ray photoelectron spectroscopic analysis (XPS) was carried out with a Kratos Axis 165 photoelectron spectroscopy system. Samples were mixed and ground together with Au powder (5% w/w) as an internal energy reference. Samples were analyzed as powders. Each sample was placed on a piece of conductive carbon tape that was adhered to a stainless-steel sample holder. Samples were introduced into the analysis chamber one at a time, and the chamber was evacuated at $\leq 10^{-8}$ Torr. No ion sputtering was performed on any of the samples. An Al monochromatic source (150 W) was used for excitation. A charge neutralizer was used to reduce the effects of differential or sample charging. The analysis area was 700 $\mu$m × 300 $\mu$m. Elemental quantification calculations were based on broad survey results from single sweeps at higher sensitivity (pass energy = 80) and were carried out with the Kratos Axis Vision processing software taking into consideration the appropriate relative sensitivity factors for the particular XPS system. High-resolution elemental scans were carried out at a lower sensitivity (pass energy = 20), using multiple sweeps to improve the signal-to-noise ratio. Deconvolution of the spectra was performed with Gaussian function fitting using the OriginPro 9.7 software package.

*4.2.5. Structural Characterization.* Scanning electron microscopy (SEM) was conducted with Au-coated samples on a Hitachi Model S-4700 field-emission microscope.

*4.2.6. Thermal Characterization.* Temperature-modulated differential scanning calorimetry (TMDSC) was conducted under $N_2$ and $O_2$ with a TA Instruments Differential Scanning Calorimetry Model Q2000 calibrated against a sapphire standard and run from 35 to 350 °C using a heating rate of 5 °C min$^{-1}$. The T4P modulation mode was used with a 60 s modulation period and 1 °C modulation amplitude.

*4.2.7. Porosity and Gas Sorption Studies.* The pore structure was probed with $N_2$-sorption porosimetry at 77 K using either Micromeritics ASAP 2020 or a TriStar II 3020 version 3.02 surface area and porosity analyzer. Before the analysis, samples were degassed for 24 h under vacuum at 80 °C. Total surface areas, $\sigma$, were determined via the Brunauer–Emmett–Teller (BET) method from the $N_2$-sorption isotherms. Micropore surface areas were calculated via t-plot analysis of the $N_2$-sorption isotherms using the Harkins and Jura model.[52] Average diameters were calculated using the $4 \times V/\sigma$ method, where the specific pore volume, $V$, was set equal either to $V_{total} = (1/\rho_b) - (1/\rho_s)$, or to $V_{max}$, which is the single highest volume of $N_2$ adsorbed along the $N_2$-sorption isotherm as $P/P_o \rightarrow 1$. Micropore analysis was conducted with low-pressure $N_2$-sorption at 77 K using the Micromeritics ASAP 2020 instrument equipped with a low-pressure transducer. Prior to low-pressure $N_2$-sorption analysis at 77 K, a third degassing step was carried out under 1 $\mu$m of Hg at 120 °C directly on the analysis port of the Micromeritics ASAP 2020 instrument. Micropore volumes, micropore size distributions, and the median micropore diameters were obtained with the Horvath–Kawazoe method applied to the low-pressure $N_2$-sorption data at 77 K, assuming pores with cylindrical geometry.[54]

## ■ ASSOCIATED CONTENT

### Supporting Information

The Supporting Information is available free of charge at https://pubs.acs.org/doi/10.1021/acs.chemmater.2c02797.

> Pathways for the HCl-catalyzed ring-opening polymerization of THQ, including the corresponding PBDAZ-240 products (Appendix I); summary of all PBDAZ-100 and PBDAZ-240 products from all pathways of Appendix I (Appendix II); $^{1}$H-$^{15}$N HSQC NMR spectrum of the THQ monomer (Appendix III); $^{15}$N NMR predictions for all products from all pathways (Appendix IV); elemental analysis data as a function of the processing conditions (Appendix V); Liquid-phase $^{1}$H, $^{13}$C NMR, and $^{13}$C APT NMR spectra of the THQ monomer and its precursors (Appendix VI) (PDF)

## ■ AUTHOR INFORMATION


### Corresponding Authors

**Nicholas Leventis** − *Department of Chemistry, Missouri S&T, Rolla, Missouri 65409, United States;* Present Address: Aspen Aerogels, 30 Forbes Road, Bldg B, Northborough, Massachusetts 01532, United States; Email: nleventis@aerogel.com

**Chariklia Sotiriou-Leventis** − *Department of Chemistry, Missouri S&T, Rolla, Missouri 65409, United States;* orcid.org/0000-0003-3283-8257; Email: cslevent@mst.edu

### Authors

**Vaibhav A. Edlabadkar** − *Department of Chemistry, Missouri S&T, Rolla, Missouri 65409, United States;* orcid.org/0000-0001-5763-7318

**Saidulu Gorla** − *Department of Chemistry, Missouri S&T, Rolla, Missouri 65409, United States*

**Rushi U. Soni** − *Department of Chemistry, Missouri S&T, Rolla, Missouri 65409, United States;* orcid.org/0000-0002-1855-8905

**A. B. M. Shaheen ud Doulah** − *Department of Chemistry, Missouri S&T, Rolla, Missouri 65409, United States*

**Joseph Gloriod** − *Department of Chemistry, Missouri S&T, Rolla, Missouri 65409, United States*

**Samuel Hackett** − *Department of Chemistry, Missouri S&T, Rolla, Missouri 65409, United States*

Complete contact information is available at: https://pubs.acs.org/10.1021/acs.chemmater.2c02797


### Notes

The authors declare no competing financial interest.

## ■ ACKNOWLEDGMENTS

The authors thank the NSF for financial support under award number CMMI-1530603 (sub-contract to MS&T from Tufts University).

## ■ REFERENCES

(1) Holly, F. W.; Cope, A. C. Condensation Products of Aldehydes and Ketones with *o*-Aminobenzyl Alcohol and *o*-Hydroxybenzylamine. *J. Am. Chem. Soc.* **1944**, *66*, 1875−1879.
(2) Ning, X.; Ishida, H. Phenolic Materials via Ring-opening Polymerization: Synthesis and Characterization of Bisphenol-A Based Benzoxazines and Their Polymers. *J. Polym. Sci., Part A: Polym. Chem.* **1994**, *32*, 1121−1129.
(3) Leventis, N.; Donthula, S. *Advanced and Emerging Polybenzoxazine Science and Technology*; Ishida, H.; Froimowicz, P., Eds.; Elsevier, 2017; pp 673−695.
(4) Alwin, S.; Shajan, X. S. Aerogels: Promising Nanostructured Materials for Energy Conversion and Storage Applications. *Mater. Renewable Sustainable Energy* **2020**, *9*, No. 7.
(5) Vareda, J. P.; Lamy-Mendes, A.; Durães, L. A Reconsideration on the Definition of the Term Aerogel Based on Current Drying Trends. *Microporous Mesoporous Mater.* **2018**, *258*, 211−216.
(6) Leventis, N.; Sadekar, A.; Chandrasekaran, N.; Sotiriou-Leventis, C. Click Synthesis of Monolithic Silicon Carbide Aerogels from Polyacrylonitrile-Crosslinked 3D Silica Networks. *Chem. Mater.* **2010**, *22*, 2790−2803.
(7) Pierre, A. C.; Rigacci, A. *Aerogels Handbook*; Aegerter, M. A.; Leventis, N.; Koebel, M. M., Eds.; Springer: New York, 2011; pp 21−45.
(8) Pierre, A. C.; Pajonk, G. M. Chemistry of Aerogels and Their Applications. *Chem. Rev.* **2002**, *102*, 4243−4266.
(9) Wordsworth, R.; Kerber, L.; Cockell, C. Enabling Martian Habitability with Silica Aerogel via the Solid-State Greenhouse Effect. *Nat. Astron.* **2019**, *3*, 898−903.
(10) Lorjai, P.; Chaisuwan, T.; Wongkasemjit, S. Porous Structure of Polybenzoxazine-based Organic Aerogel Prepared by Sol−gel Process and their Carbon Aerogels. *J. Sol-Gel Sci. Technol.* **2009**, *52*, 56−64.
(11) Lorjai, P.; Wongkasemjit, S.; Chaisuwan, T.; Jamieson, A. M. Significant Enhancement of Thermal Stability in the Non-oxidative Thermal Degradation of Bisphenol-A/aniline Based Polybenzoxazine Aerogel. *Polym. Degrad. Stab.* **2011**, *96*, 708−178.
(12) Sadekar, A. G.; Mahadik, S. S.; Bang, A.; Larimore, Z. J.; Wisner, C.; Bertino, M. F.; Kalkan, A. K.; Mang, J. T.; Sotiriou-Leventis, C.; Leventis, N. From 'Green' Aerogels to Porous Graphite by Emulsion Gelation of Acrylonitrile. *Chem. Mater.* **2012**, *24*, 26−47.
(13) Soni, R. U.; Edlabadkar, V. A.; Rewatkar, P. M.; ud Doulah, A. B. M. S.; Leventis, N.; Sotiriou-Leventis, C. Low-Temperature Catalytic Synthesis of Graphite Aerogels from Polyacrylonitrile-Crosslinked Iron Oxide and Cobalt Oxide Xerogel Powders. *Carbon* **2022**, *193*, 107−127.
(14) Mahadik-Khanolkar, S.; Donthula, S.; Sotiriou-Leventis, C.; Leventis, N. Polybenzoxazine Aerogels. 1. High-Yield Room-Temperature Acid-Catalyzed Synthesis of Robust Monoliths, Oxidative Aromatization, and Conversion to Microporous Carbons. *Chem. Mater.* **2014**, *26*, 1303−1317.
(15) Mahadik-Khanolkar, S.; Donthula, S.; Bang, A.; Wisner, C.; Sotiriou-Leventis, C.; Leventis, N. Polybenzoxazine Aerogels. 2. Interpenetrating Networks with Iron Oxide and the Carbothermal Synthesis of Highly Porous Monolithic Pure Iron(0) Aerogels as Energetic Materials. *Chem. Mater.* **2014**, *26*, 1318−1331.
(16) Malakooti, S.; Qin, G.; Mandal, C.; Soni, R.; Taghvaee, T.; Ren, Y.; Chen, H.; Tsao, N.; Shiao, J.; Kulkarni, S. S.; Sotiriou-Leventis, C.; Leventis, N.; Lu, H. Low-Cost, Ambient-Dried, Superhydrophobic, High Strength, Thermally Insulating, and Thermally Resilient Polybenzoxazine Aerogels. *ACS Appl. Polym. Mater.* **2019**, *1*, 2322−2333.
(17) Leventis, N.; Sotiriou-Leventis, C.; Donthula, S.; Churu, G.; Lu, H.; Mahadik-Khanolkar, S. Organic and Metallic Aerogels, Compositions for the Organic and Metallic Aerogels, and Methods for Manufacturing the Organic and Metallic Aerogels. U.S. Patent US11,104,764, Aug 31, 2021.
(18) Li, H.; Li, J.; Thomas, A.; Liao, Y. Ultra-High Surface Area Nitrogen-Doped Carbon Aerogels Derived from a Schiff-Base Porous Organic Polymer Aerogel for $CO_2$ Storage and Supercapacitors. *Adv. Funct. Mater.* **2019**, *29*, No. 1904785.
(19) Geng, S.; Wei, J.; Jonasson, S.; Hedlund, H.; Oksman, K. Multifunctional Carbon Aerogels with Hierarchical Anisotropic Structure Derived from Lignin and Cellulose Nanofibers for $CO_2$ Capture and Energy Storage. *ACS Appl. Mater. Interfaces* **2020**, *12*, 7432−7441.
(20) Soni, R. U.; Edlabadkar, V. A.; Greenan, D.; Rewatkar, P. M.; Leventis, N.; Sotiriou-Leventis, C. Preparation of Carbon Aerogels from Polymer-Cross-Linked Xerogel Powders without Supercritical Fluid Drying and Their Application in Highly Selective $CO_2$ Adsorption. *Chem. Mater.* **2022**, *34*, 4828−4847.
(21) Majedi Far, H.; Rewatkar, P. M.; Donthula, S.; Taghvaee, T.; Saeed, A. M.; Sotiriou-Leventis, C.; Leventis, N. Exceptionally High $CO_2$ Adsorption at 273 K by Microporous Carbons from Phenolic Aerogels: The Role of Heteroatoms in Comparison with Carbons from Polybenzoxazine and Other Organic Aerogels. *Macromol. Chem. Phys.* **2019**, *220*, No. 1800333.
(22) Wang, H.; Shao, Y.; Mei, S.; Lu, Y.; Zhang, M.; Sun, J.; Matyjaszewski, K.; Antonietti, M.; Yuan, J. Polymer-Derived Heteroatom-Doped Porous Carbon Materials. *Chem. Rev.* **2020**, *120*, 9363−9419.
(23) Lim, G.; Lee, K. B.; Ham, H. C. Effect of N-Containing Functional Groups on $CO_2$ Adsorption of Carbonaceous Materials: A Density Functional Theory Approach. *J. Phys. Chem. C* **2016**, *120*, 8087−8095.
(24) Babu, D. J.; Bruns, M.; Schneider, R.; Gerthsen, D.; Schneider, J. J. Understanding the Influence of N-Doping on the $CO_2$ Adsorption Characteristics in Carbon Nanomaterials. *J. Phys. Chem. C* **2017**, *121*, 616−626.
(25) Wei, R.; Dai, X.; Shi, F. Enhanced $CO_2$ Adsorption on Nitrogen-Doped Carbon Materials by Salt and Base Co-Activation Method. *Materials* **2019**, *12*, 1207.
(26) Alabadi, A.; Abbood, H. A.; Li, Q.; Jing, N.; Tan, B. Imine-Linked Polymer Based Nitrogen-Doped Porous Activated Carbon for Efficient and Selective $CO_2$ Capture. *Sci. Rep.* **2016**, *6*, No. 38614.
(27) Titirici, M. M.; White, R. J.; Zhao, L. Nitrogen-doped Hydrothermal Carbons. *Green* **2012**, *2*, 25−40.
(28) Shen, W.; Fan, W. Nitrogen-Containing Porous Carbons: Synthesis and Application. *J. Mater. Chem. A* **2013**, *1*, 999−1013.
(29) Li, J.; Chen, J.; Gui, C.; Zhang, L.; Qin, Y.; Xu, Q.; Zhang, J.; Liu, H.; Shen, X.; Jiang, H. Discovering Novel Chemical Inhibitors of Human Cyclophilin A: Virtual Screening, Synthesis, and Bioassay. *Bioorg. Med. Chem.* **2006**, *14*, 2209−2224.
(30) Huang, G.; Roos, D.; Stadtmüller, P.; Decker, M. A Simple Heterocyclic Fusion Reaction and its Application for Expeditious Syntheses of Rutaecarpine and its Analogs. *Tetrahedron Lett.* **2014**, *55*, 3607−3609.
(31) Reddy, L. M.; Reddy, P. P.; Reddy, P. S. N. Synthesis of 6,6′-methylenebisquinazolinones and 7,7′-methylenebis-1,4-benzodiazepine-2,5-diones. *Indian J. Chem. Sect. B* **2002**, *41B*, 2405−2409.
(32) Sotiriou-Leventis, C.; Mao, Z.; Rawashdeh, A. M. A Convenient Synthesis and Spectroscopic Characterization of *N*,*N*′-Bis(2-propenyl)-2,7-diazapyrenium Quaternary Salts. *J. Org. Chem.* **2000**, *65*, 6017−6023.
(33) Shriner, R. L.; Hermann, C. K. F.; Morrill, T. C.; Curtin, D. Y.; Fuson, R. C. *The Systematic Identification of Organic Compounds*, 7th ed.; John Wiley & Sons: New York, 1998; Chapter 6, pp 126−154.
(34) Huang, R.; Carson, S. O.; Silva, J.; Aga, T.; Ishida, H.; Maia, J. M. Interplay Between Rheological and Structural Evolution of Benzoxazine Resins During Polymerization. *Polymer* **2013**, *54*, 1880−1886.

(35) Ishida, H.; Sanders, D. P. Regioselectivity and Network Structure of Difunctional Alkyl-Substituted Aromatic Amine-Based Polybenzoxazines. *Macromolecules* **2000**, *33*, 8149−8157.
(36) Wang, Y. X.; Ishida, H. Cationic Ring-opening Polymerization of Benzoxazines. *Polymer* **1999**, *40*, 4563−4570.
(37) Silverstein, R. M.; Webster, F. X.; Kiemle, D. J. *Spectrometric Identification of Organic Compounds*, 7th ed.; John Wiley & Sons: New York, 2005; Chapter 2, pp 72−126.
(38) Dunkers, J.; Ishida, H. Vibrational Assignments of 3-alkyl-3,4-dihydro-6-methyl-2H-1,3-Benzoxazines in the Fingerprint Region. *Spectrochim. Acta* **1995**, *51A*, 855−867.
(39) Lukasiewicz, M.; Bogdal, D.; Pielichowski, J. Microwave Assisted Oxidation of Side Chain Arenes by Magtrieve. *Adv. Synth. Catal.* **2003**, *345*, 1269−1272.
(40) Jeon, K. O.; Jun, J. H.; Yu, J. S.; Lee, C. K. Infrared and Nuclear Magnetic Resonance Properties of Benzoyl Derivatives of Five-membered Monoheterocycles and Determination of Aromaticity Indices. *J. Heterocycl. Chem.* **2003**, *40*, 763−771.
(41) Jackman, L. M.; Trewella, J. C. The Use of $^{13}C$ Spin Lattice Relaxation Times for Determining the Position of the Proton in an Intramolecular Hydrogen Bond. *J. Am. Chem. Soc.* **1976**, *98*, 5712−5714.
(42) Li, H.; Zhu, R.-Y.; Shi, W.-J.; He, K.-H.; Shi, Z. J. Synthesis of Fluorenone Derivatives through Pd-Catalyzed Dehydrogenative Cyclization. *Org. Lett.* **2012**, *14*, 4850−4853.
(43) Saeed, A. M.; Rewatkar, P. M.; Majedi Far, H.; Taghvaee, T.; Donthula, S.; Mandal, C.; Sotiriou-Leventis, C.; Leventis, N. Selective $CO_2$ Sequestration with Monolithic Bimodal Micro/Macroporous Carbon Aerogels Derived from Stepwise Pyrolytic Decomposition of Polyamide-Polyimide-Polyurea Random Copolymers. *ACS Appl. Mater. Interfaces* **2017**, *9*, 13520−13536.
(44) Bodenhausen, G.; Ruben, D. J. Natural Abundance Nitrogen-15 NMR by Enhanced Heteronuclear Spectroscopy. *Chem. Phys. Lett.* **1980**, *69*, 185−189.
(45) Goward, G. R.; Shnell, I.; Brown, S. P.; Spiess, H. W.; Kim, H. D.; Ishida, H. Investigation of a NH Hydrogen Bond in a Solid Benzoxazine Dimer by $^{1}H-^{15}N$ NMR Correlation Techniques under Fast Magic Angle Spinning. *Magn. Reson. Chem.* **2001**, *39*, S5−S17.
(46) López, G. P.; Castner, D. G.; Ratner, B. D. XPS O 1s Binding Energies for Polymers Containing Hydroxyl, Ether, Ketone and Ester Groups. *Surf. Interface Anal.* **1991**, *17*, 267−272.
(47) Kim, C. M.; Jeong, H. S.; Kim, E. H. NEXAFS and XPS Characterization of Molecular Oxygen Adsorbed on Ni(100) at 80 K. *Surf. Sci.* **2000**, *459*, L457−L461.
(48) Figueiredo, J. L.; Pereira, M. F. R. The Role of Surface Chemistry in Catalysis with Carbons. *Catal. Today* **2010**, *150*, 2−7.
(49) Chen, J.; Mao, Z.; Zhang, L.; Tang, Y.; Wang, D.; Bie, L.; Fahlman, B. D. Direct Production of Nitrogen-Doped Porous Carbon from Urea via Magnesiothermic Reduction. *Carbon* **2018**, *130*, 41−47.
(50) Inagaki, M.; Toyoda, M.; Soneda, Y.; Morishita, T. Nitrogen-Doped Carbon Materials. *Carbon* **2018**, *132*, 104−140.
(51) McKeown, N. B.; Budd, P. M.; Msayib, K. J.; Ghanem, B. S.; Kingston, H. J.; Tattershall, C. E.; Makhseed, S.; Reynolds, K. J.; Fritsch, D. Polymers of Intrinsic Microporosity (PIMS): Bridging the Void Between Microporous and Polymeric Materials. *Chem. - Eur. J.* **2005**, *11*, 2610−2620.
(52) Harkins, W. D.; Jura, G. Surfaces of Solids. XIII. A Vapor Adsorption Method for the Determination of the Area of a Solid without the Assumption of a Molecular Area, and the Areas Occupied by Nitrogen and Other Molecules on the Surface of a Solid. *J. Am. Chem. Soc.* **1944**, *66*, 1362−1373.
(53) Webb, P. A.; Orr, C. *Analytical Methods in Fine Particle Technology*; Micromeritics Instrument Corporation: Norcross, GA, 1997; pp 81−87.
(54) Horváth, G.; Kawazoe, K. Method for the Calculation of Effective Pore Size Distribution in Molecular Sieve Carbon. *J. Chem. Eng. Jpn.* **1983**, *16*, 470−475.




https://doi.org/10.1021/acs.chemmater.2c02797
*Chem. Mater.* 2023, 35, 432−446